Ultramicroscopy 37 (1991) 14–38
North-Holland

High-resolution Z-contrast imaging of crystals

S.J. Pennycook and D.E. Jesson

Solid State Division, Oak Ridge National Laboratory Oak Ridge, TN 37831-6024, U.S.A.

Received 27 December 1990

The use of a high-angle annular detector in a scanning transmission electron microscope is shown to provide incoherent images of crystalline materials with strong compositional sensitivity. How this occurs, even in the presence of strong dynamical diffraction of the low-angle beams, becomes very clear in a Bloch wave description of the imaging, which shows that only tightly bound *s*-type Bloch states contribute significantly to the image. Interference effects are therefore precluded and the image can be described as a convolution. There are no contrast reversals with thickness or defocus and no Fresnel fringe effects at interfaces. Each atomic column contributes to the image independently of its neighbors until the *s*-states themselves overlap. With an optimum imaging probe the nature of the convolution can be visualized intuitively to a scale well below the resolution limit. To first order, therefore, each object has only one possible image, and since the same probe is used for all objects, an unknown structure can be interpreted directly. These ideas will be illustrated with images from semiconductors, superconductors, and alloys.

1. Introduction

The scanning transmission electron microscope (STEM) differs significantly from its conventional counterpart since in order to form an image of a specimen it is not necessary to refocus scattered electrons. The image is formed simply by detecting the electron flux scattered in some direction (or indeed any other signal) as a function of probe position. Therefore, it becomes a simple matter to include electrons scattered through angles considerably larger than the scattering angles employed in a conventional TEM, increasing both the efficiency of the imaging process as well as the atomic number or Z sensitivity. It was this realization that motivated the original development of STEM by Crewe and his coworkers [1,2]. Specifically, an annular detector was employed having an inner angle just greater than the optimum objective aperture angle and a large outer angle. This could collect up to 90% of the total elastic scattering to provide more efficient imaging of beam-sensitive biological materials than conventional bright or dark field microscopy, together with strong Z contrast through the $Z^{3/2}$ dependence of the total elastic scattering cross section. Spectacular images were obtained of single heavy atoms supported on thin carbon support films, and ratio techniques were employed to reduce the contribution of the substrate. Certain incoherent characteristics were noted, in particular the improved image resolution and freedom from contrast reversals [3] even, apparently, from clusters of atoms many spacings across and several layers thick [4], and so it has sometimes proved tempting to describe the STEM entirely as an incoherent imaging device [5]. However, if low-angle scattering contributes to the image this is not true in general, and quantitative image calculations need to be based on coherent scattering theory [3,6,7]. Relatively few STEM images were taken from the thicker crystals commonly studied by conventional high-resolution electron microscopy [8]. If low-order diffracted beams reach the detector the image is dominated by coherent scattering, and such images can be considered to arise from interference between overlapping diffraction discs on the annular detector [9]. Strong dynamical diffraction effects can

0304-3991/91/$03.50

occur including contrast reversals so that interpretation is non-intuitive, with the result that there is little reason for choosing this imaging mode compared to conventional TEM imaging with its significantly better signal-to-noise ratio. We will see that only by increasing the inner detector angle so that the image is formed predominantly from incoherent scattering do we obtain an image which shows almost perfect incoherent characteristics, and which can therefore be interpreted intuitively to first order.

The idea for the high-angle annular detector arose out of attempts to extend the Crewe ratio techniques to the imaging of small catalyst particles. With bright-field imaging it is difficult to reliably distinguish a particle approaching the resolution limit from the speckle pattern of an amorphous support or from small diffracting regions in a polycrystalline support. Larger particles (2 nm and above) themselves showed strong diffraction contrast effects, with the result that Z contrast was swamped by contrast variations due to crystallite orientation, which were only enhanced on forming a ratio. Howie, therefore, suggested excluding the Bragg reflections from reaching the detector by increasing its inner detector angle [10]. Coherent Bragg diffraction would be replaced with thermal diffuse scattering and contrast changes due to crystallite orientation would be reduced to those resulting from channeling effects of the incident beam. The compositional sensitivity would be increased by avoiding the low-angle scattering toward the Z^2 dependence of unscreened Rutherford scattering. Despite the reduced efficiency of only collecting a fraction of the total elastic scattering, the high-angle detector has proved extremely successful for catalyst studies [11]. Furthermore, with single-crystal samples an orientation can be chosen far from any strong Bragg reflections so that channeling effects can be avoided entirely. In this case, the image represents an elemental map which can be directly quantified using appropriate cross sections. This form of Z-contrast imaging has been described in detail previously and led to the idea of attempting to resolve the crystal structure directly [12].

In the present paper we return to the question of high-resolution imaging and show how the high-angle detector can provide a high-resolution image showing predominantly incoherent characteristics and compositional sensitivity over a wide range of sample thickness. We use a Bloch wave approach, even if it is not computationally the most efficient, since it provides two important advantages. Firstly, it presents a clear physical picture of how the incoherent characteristics arise, even in the presence of strong dynamical diffraction of the STEM probe. The high-angle detector effectively acts as a Bloch state filter, the image being formed predominantly from s-type states bound to atomic strings. Due to their symmetry such states place a high intensity at the atom sites where scattering to the high-angle detector is localized. Since they are tightly bound, contributions from all angles contained in the STEM probe add coherently. Therefore, the s-states are responsible for practically the entire image contrast. The Bloch state approach also provides a convenient description of the object function, including the effects of absorption, for any sample thickness. It is simply the thickness-integrated s-state intensity at the atom sites. With an object consisting of different types of strings their relative image intensity will therefore change somewhat with thickness, but can be quantitatively and easily predicted by the Bloch wave approach, which provides a second major advantage.

Since the tightly bound s-states are relatively insensitive to surrounding strings or amorphous material, images of interfaces, superlattices, or complex unit cell materials are as simple to predict as perfect crystals. Their object functions can be assembled "column by column" from individual strings and convoluted with the probe to form the image. Differences in s-state excitation and absorption tend to be weak compared to differences in the scattering cross section with the result that to first order images can be predicted and interpreted intuitively, even on a scale below the resolution limit. These ideas will be illustrated with a number of examples taken mostly from studies of semiconducting and superconducting materials. All images presented here were obtained using a VG Microscopes HB501UX STEM operating at 100 kV and equipped with an ultra-high-resolution objective lens pole piece with

spherical aberration coefficient (C_s) of 1.3 mm. The theoretical probe full-width half-maximum (FWHM) intensity is 2.2 Å, which has been confirmed in practice by imaging single uranium atoms supported on a thin carbon film [13].

2. High-angle electron scattering

Obviously as we become concerned with higher scattering angles, thermal diffuse scattering will become increasingly important, eventually dominating the scattering. The simplest description of thermal diffuse scattering is based on the Einstein model of independently vibrating atoms treated as harmonic oscillators with a mean-square vibration amplitude $\overline{u^2}$. Time-averaging the instantaneous projected potential leads to the usual result that the intensity of coherent Bragg reflections is reduced by the Debye–Waller factor e^{-2Ms^2}, where $M = 8\pi^2\overline{u^2}$, and $s = \theta_B/\lambda$, where θ_B is the Bragg angle and λ the electron wavelength. The lost intensity is redistributed uniformly between the Bragg spots (see, e.g., Hall and Hirsch [14]). This model is a true incoherent model since correlations between the atomic vibrations (phonon effects) are ignored. A phonon model changes the amount and the form of the redistribution quite significantly at low angles, but it was shown very clearly by Hall [15] that high-angle thermal diffuse scattering contains very little single phonon contribution, the importance of multi-phonon scattering (the simultaneous creation or destruction of multiple phonons in a single scattering event) increasing rapidly with increasing s. As more phonons contribute to the scattering, it becomes much less dependent on incident beam orientation and peaks less around the reciprocal lattice points, until at sufficiently large s it becomes identical to the distribution of diffuse intensity predicted by the Einstein model. In particular, we note that a single phonon model will underestimate the high-angle thermal diffuse intensity by at least an order of magnitude. Image calculations based on single phonon scattering [16,17], therefore, greatly overestimate the contribution of coherent scattering to the high-angle signal. Besides being valid at high angles, the Einstein model is also useful for low-angle scattering if the details of the angular distribution are not important. For example, it gives quite reasonable estimates of the integrated diffuse scattering needed in the treatment of absorption [15,18].

Within an Einstein model, each atom is therefore considered as an independent generator of diffuse scattering with a cylindrically symmetric distribution about the incident beam direction. Kikuchi lines arise through the diffraction of the outgoing electrons, although the total scattered intensity is conserved [19–22]. An absorption

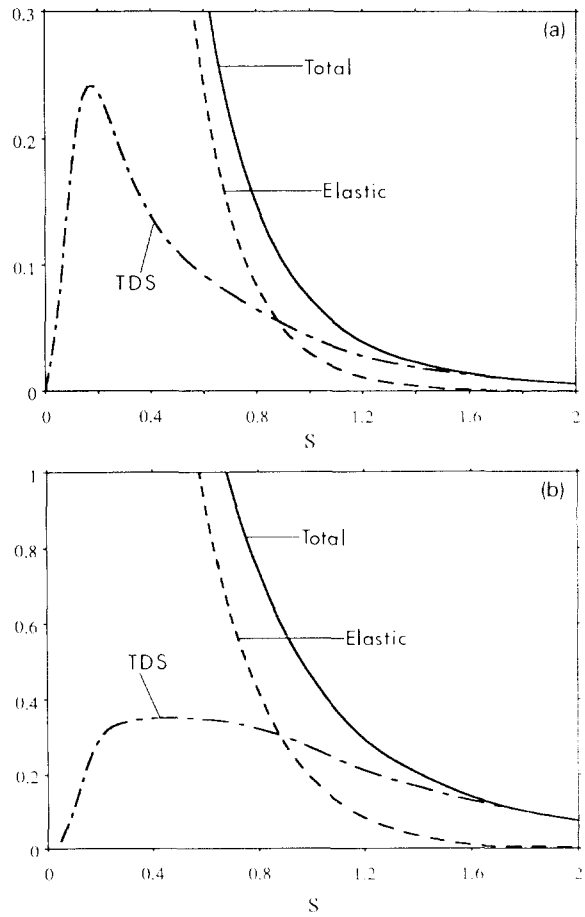

Fig. 1. Plots of the total, elastic, and thermal diffuse scattering (TDS) from an isolated Si atom at room temperature, (a) per unit solid angle, (b) integrated over a narrow annulus at s, calculated with Doyle–Turner parameters [26] and $M = 0.45$. In our case, the high-angle detector covers approximately $s = 1$–2 (75–150 mrad).

coefficient can be defined (due to thermal diffuse scattering) without considering the redistribution of the outgoing electron flux since little diffuse scattering passes through typical microscope objective apertures (see fig. 1). To a good approximation the intensity absorbed is just the total diffuse intensity, which is conserved, and the loss to the transmitted beam can be treated in the standard way by adding an imaginary component $iV'(\boldsymbol{R})$ to the lattice potential $V(\boldsymbol{R})$ [23], giving a total potential

$$V_{\text{tot}}(\boldsymbol{R}) = V(\boldsymbol{R}) + iV'(\boldsymbol{R}). \tag{1}$$

Here, the potentials are all projected quantities written explicitly in terms of the two-dimensional position vector $\boldsymbol{R}$, which is normal to the zone-axis direction z. The imaginary potential leads to a rate of loss of electrons (production of thermal diffuse scattering) given by

$$I^{\text{TDS}} = \frac{2}{\hbar v}\int |\psi(\boldsymbol{r})|^2 V'(\boldsymbol{R})\,\mathrm{d}\boldsymbol{r}, \tag{2}$$

where $\psi(\boldsymbol{r})$ is the total electron wave function and v the electron velocity. The Fourier components of the absorptive potential are given by (see, e.g., Bird and King [24])

$$V_g' = \frac{-\hbar^2}{2m_0}\frac{4\pi}{\Omega}\sum_{\kappa} \mathrm{e}^{-\mathrm{i}\boldsymbol{g}\cdot\boldsymbol{r}_\kappa} f_\kappa'(s, M)\,\mathrm{e}^{-M_\kappa s^2}, \tag{3}$$

while those of the real lattice potential are given by

$$V_g = \frac{-\hbar^2}{2m_0}\frac{4\pi}{\Omega}\sum_{\kappa} \mathrm{e}^{-\mathrm{i}\boldsymbol{g}\cdot\boldsymbol{r}_\kappa} f_\kappa^{\mathrm{B}}(s)\,\mathrm{e}^{-M_\kappa s^2}. \tag{4}$$

Here, f_κ^{B} are the atomic scattering factors calculated in the first Born approximation (see Humphreys [25]) which are tabulated, for example, by Doyle and Turner [26] as a function of $s = g/4\pi$. In each case $\boldsymbol{r}_\kappa$ describes the stationary lattice position of atom κ in the unit cell of volume Ω and m_0 is the electron rest mass. The absorptive form factor $f_\kappa'(s, M)$ can be defined in terms of the elastic form factor $f_\kappa(s)$

$$f_\kappa'(s, M) = \frac{2h}{m_0 v}\int f_\kappa(|\boldsymbol{s}'|) f_\kappa(|\boldsymbol{s}-\boldsymbol{s}'|) \times\left[1-\mathrm{e}^{-2M_\kappa(s'^2-\boldsymbol{s}\cdot\boldsymbol{s}')}\right]\mathrm{d}^2\boldsymbol{s}', \tag{5}$$

involving a two-dimensional integration over the reflecting sphere. It is also usual to use the first Born approximation values here for the atomic scattering amplitudes [24,27,28], although this is not strictly valid for the heavier elements particularly at higher scattering angles.

For a plane incident wave the scattering involves only V_0' and $f_\kappa'(0, M)$. In this case, the integrand in eq. (5) becomes $f_\kappa^2(s')[1-\mathrm{e}^{-2M_\kappa s'^2}]$, which is just the diffuse scattering distribution from an isolated atom, the difference between the elastic scattering from a stationary atom and a vibrating atom, as illustrated in fig. 1. This distribution initially increases with s due to the decreasing Debye–Waller factor, and then turns over due to the decreasing elastic form factor. Thus, the ratio of the Fourier coefficients V_g'/V_g initially increases with g [29], i.e., the absorptive potential is sharper in real space than the corresponding elastic potential.

The case of the high-angle annular detector can be treated in a similar fashion. Again, we can ignore diffraction of the outgoing electrons since, although we do not detect the total diffuse scattering (see fig. 1), we detect a constant representative fraction. The detector covers an angular range which is large compared to the widths of Kikuchi lines, and with a crystal in a zone axis orientation, the strongest Kikuchi lines extend radially and so redistribute flux tangentially to the detector. Therefore, negligible error results from ignoring the redistribution of the outgoing electrons and treating the high-angle signal through an absorptive potential $V^{\mathrm{HA}}(\boldsymbol{R})$, where

$$V_g^{\mathrm{HA}} = \frac{-\hbar^2}{2m_0}\frac{4\pi}{\Omega}\sum_{\kappa} \mathrm{e}^{-\mathrm{i}\boldsymbol{g}\cdot\boldsymbol{r}_\kappa} f_\kappa^{\mathrm{HA}}(s, M)\,\mathrm{e}^{-M_\kappa s^2} \tag{6}$$

and

$$f_\kappa^{\mathrm{HA}}(s, M) = \frac{2h}{m_0 v}\int_{\text{detector}} f_\kappa(|\boldsymbol{s}'|) f_\kappa(|\boldsymbol{s}-\boldsymbol{s}'|) \times\left[1-\mathrm{e}^{-2M_\kappa(s'^2-\boldsymbol{s}\cdot\boldsymbol{s}')}\right]\mathrm{d}^2\boldsymbol{s}', \tag{7}$$

which is exactly analogous to eqs. (4) and (5), except that we have now restricted the range of the integration in (7) to the annular detector. For

$s = 0$ eq. (7) therefore represents that fraction of the total diffuse scattering from an isolated atom which reaches the detector. For finite s, the contributions to the integrands in eqs. (5) and (7) are negative inside a circle having s as its diameter, so that the components of the total absorptive potential V_g' decrease with increasing g (albeit more slowly than the elastic components V_g). If we restrict the range of integration to the detector, negative contributions can only appear for $s > s_1$, where s_1 is the inner detector cut-off, so that the instantaneous atomic potential for high-angle scattering is very much more localized than either the total absorptive potential or the elastic potential, as we would expect. Thermal averaging then introduces the usual Debye–Waller factors in eq. (6), attenuating the high-order Fourier components.

If we now examine the relative scales of the instantaneous high-angle potential, the thermally smeared high-angle potential, and the electron wavefunction, some significant simplifications can be made. The intrinsic width of the instantaneous high-angle potential is of the order of $1/4\pi s_1 \approx 0.08$ Å for our detector, which is significantly sharper than the spatial variation of the wavefunction. This is true even with s-states, which we shall find to be the most important contributors to the image, having a halfwidth of 0.35 Å in the case of Si⟨110⟩ at room temperature. Therefore, for the important Fourier components implicated in eq. (2) we have $s' \gg s$ and eq. (7) simplifies to

$$f_\kappa^{\mathrm{HA}}(s, M) \approx \frac{2h\gamma^2}{m_0 v^2} \int_{\text{detector}} f_\kappa^2(s') \left[1 - \mathrm{e}^{-2M_\kappa s'^2}\right] \mathrm{d}^2 s', \quad (8)$$

where the right-hand side is now independent of s and depends only on detector geometry. This is just the approximation of complete localization, where each atom is considered as a δ-function source of diffuse intensity located at the instantaneous atom position, the strength of the source depending on detector angle. It must always be a good approximation since the high-angle potential is always much sharper than the elastic potential, which determines the spatial variation of the wave function. In fact, these arguments can be extended to include the thermal averaging itself. Since the total absorptive potential $V'(\boldsymbol{R})$ is sharper than the thermally smeared elastic potential $V(\boldsymbol{R})$, the root-mean-square atomic vibration amplitude is generally smaller than the width of the s-state. For the Si case $(\overline{u^2})^{1/2} \approx 0.08$ Å, comparable to the width of the instantaneous high-angle potential, and so representing the thermally smeared high-angle potential as a δ-function located at the lattice sites $\boldsymbol{r}_\kappa$ is also a good approximation. The accuracy of these approximations and the temperature dependence of the image will be discussed in detail elsewhere [30]. Here we simply note that if much of the total elastic scattering is diffuse scattering (see fig. 1 and eq. (8)), then σ_κ will be close to its full isolated atom cross section. Increasing the temperature will broaden $V^{\mathrm{HA}}(\boldsymbol{R})$ and eventually the s-states themselves, leading to a reduced signal. Conversely, decreasing the temperature will increase the high-angle intensity, although naturally the total absorption will decrease. We note also that the projected potential $V^{\mathrm{HA}}(\boldsymbol{R})$ is peaked at the atom sites whether or not the δ-function approximation is made. The Einstein model always gives the high-angle behavior correctly, which is not true for phonon models if either a single phonon model or other small-angle approximation is made (see, e.g., Takagi [31]). While these approximations may be valid in many cases, care must be taken not to extrapolate such treatments into the high-angle regime. The statement by Wang [17], for example, that the absorptive potential is zero at the atom sites is clearly in error. High-angle scattering is dominated by multiphonon processes whether a Debye or an Einstein dispersion relation is used [15,18].

If we adopt the δ-function approximation we can replace the integral in eq. (2) by a simple sum over the atom sites

$$I^{\mathrm{HA}} = \sum_\kappa |\psi(\boldsymbol{r}_\kappa)|^2 \sigma_\kappa, \quad (9)$$

where σ_κ is a high-angle atomic cross section given by

$$\sigma_\kappa = \left(\frac{4\pi\gamma}{\chi}\right)^2 \int_{\text{detector}} f_\kappa^2(s) \left[1 - \mathrm{e}^{-2M_\kappa s^2}\right] \mathrm{d}^2 s, \quad (10)$$

$\gamma = m/m_0$ and $\chi = 2\pi/\lambda$. It is important to re-

member that the σ and f_κ^{HA} are atomic properties determined by the full single-atom scattering factors f_κ, not the Born approximation values. At the angles we are concerned with it is well known that the Born approximation fails badly, particularly for the heavier elements [32], and this can cause errors by a factor of two or more in calculations of σ_κ. We therefore use a method proposed by Fleischmann [33], which gives a good fit to experimental cross section ratios [12]. Explicit expressions for σ_κ may be found in [12]. As mentioned earlier, the high-angle contribution to the total absorption is small and for calculating the electron intensity we include absorption by the method described by Bird and King [24] using the usual Doyle–Turner parameters. However, our images are quite sensitive to the absorption model used and it may be necessary to use form factors calculated beyond the first Born approximation to determine the total absorption accurately, particularly near the atom sites.

We now turn to the question of the coherent scattering reaching the annular detector. Clearly, this can be reduced to an arbitrary level by increasing the inner detector angle sufficiently, through the action of the Debye–Waller factor. Treacy [34], for example, proposed that the inner detector angle θ_1 be chosen so that $e^{-2M_\kappa s^2} \lesssim 0.02$, which would ensure that no matter what the crystal orientation the image would be dominated by thermal diffuse scattering. However, for Si at room temperature this requires an inner detector angle in excess of 150 mrad, resulting in a significant loss in imaging efficiency. We might expect, however, that with a crystal in a zone axis orientation this angle could be reduced substantially due to the curvature of the Ewald sphere. The excitation of the zero-layer coherent reflections is greatly reduced, and only the higher-order Laue zone (HOLZ) reflections are at the Bragg condition, and these are intrinsically weak. A very approximate estimate of the total HOLZ intensity in the nth ring can be obtained simply from the relevant structure factors (see, e.g., Bird [35]). Assuming a monatomic lattice with a typical Debye–Waller factor of 0.5 and ignoring screening effects the ratio of the HOLZ intensity to the diffuse intensity reaching a detector with inner angle g_1 is given by $g_1/\sqrt{2}(\chi n g_z)^{3/2} g_x$ where g_x, g_z are reciprocal lattice vectors normal and parallel to the beam. Inserting typical values $n = 1$, $g_1 = 4\pi$, $g_x = g_z = 2$ Å^{-1} and $\chi = 170$ Å^{-1} gives a value of 0.01. Although this is a very rough estimate, and assumes that both the HOLZ and diffuse scattering will be similarly enhanced by the zero-layer Bloch states, it does indicate that in general for the HOLZ reflections to dominate the image, as suggested by Spence et al. [36], a very narrow annular detector around the HOLZ ring would be required and a cooled specimen. The contrast expected for such an image would then need to be carefully considered [30,37].

In practice it is a simple matter to test experimentally the contribution of the HOLZ reflections to the image. Fig. 2 shows selected-area patterns obtained from Si on the STEM using the bright-field detector with a large collector aperture and the high-angle annular detector. The first is similar to a conventional convergent-beam pattern and the HOLZ rings are clearly visible. Line traces across these patterns can be used to estimate the total HOLZ intensity, and in the case of Si⟨110⟩ this was found to be below 1%, as expected. For Si⟨111⟩, the first HOLZ ring moves inwards due to the smaller g_z and no longer reaches the annular detector. The patterns shown on the right of fig. 2 represent angular plots of the total intensity reaching the annular detector, which we refer to as large-angle channeling patterns since most of the features can be understood as variations in the electron intensity at the atom sites with incident beam direction. Direct Bragg reflection will only show lines if the scattered intensity is significant compared to the total intensity reaching the detector. Since we see no HOLZ lines in the center of the patterns this is another indication that three-dimensional diffraction is not contributing significantly to the detected intensity for either zone axis. (For large incident beam angles we do, however, see direct diffraction in the form of long straight lines.) The large-angle channeling pattern is in practice an excellent way to orient the sample for high-resolution imaging. The zone axis is clearly visible in the pattern and moves with the sample like a Kikuchi pattern although it is formed even in thin regions of the crystal.

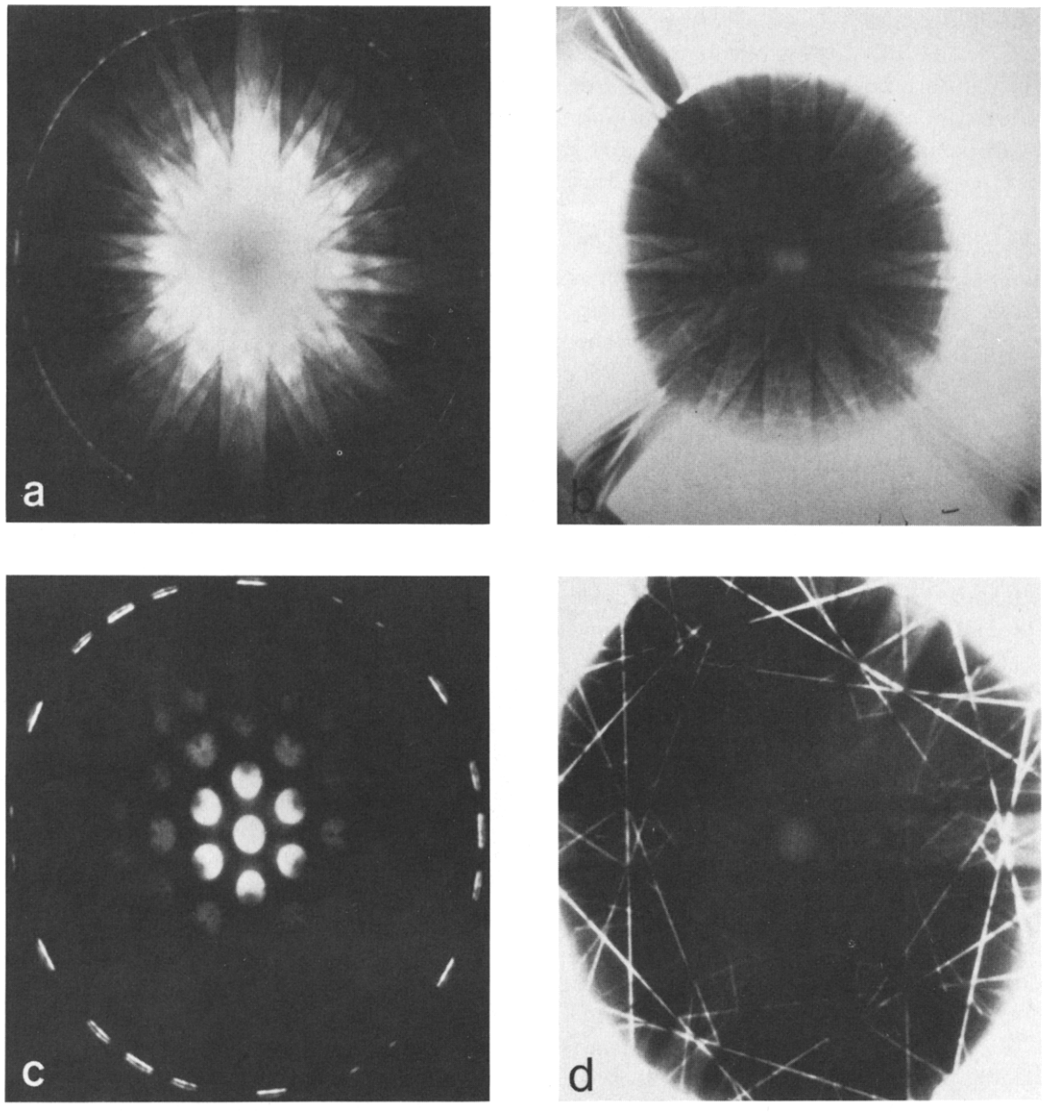

Fig. 2. Convergent-beam patterns (left) and large-angle channeling patterns (right) obtained from Si⟨110⟩ (upper) and Si⟨111⟩ (lower) using selected-area diffraction mode on the STEM. Both patterns indicate negligible HOLZ contribution to the high-angle signal.

The behavior of the zero-layer coherent reflections reaching the high-angle detector is rather interesting. Calculations have shown that the form of the image is similar in many ways to that expected from the diffuse scattering [37–40]. Strong Z contrast arises since high-angle structure factors are involved and no contrast reversals occur. This can be understood as an effective transverse incoherence [37,38]. Redistribution of the coherent scattering due to interactions between atomic columns will occur in the diffraction plane on the scale of low-order reflections g_x. Since the inner detection angle $g_1 \gg g_x$ and the detector covers a wide angular range, this redistribution is on a scale very much finer than the scale of the detector. The coherent interactions between columns, therefore, do not affect the total intensity reaching the detector and we have an effective

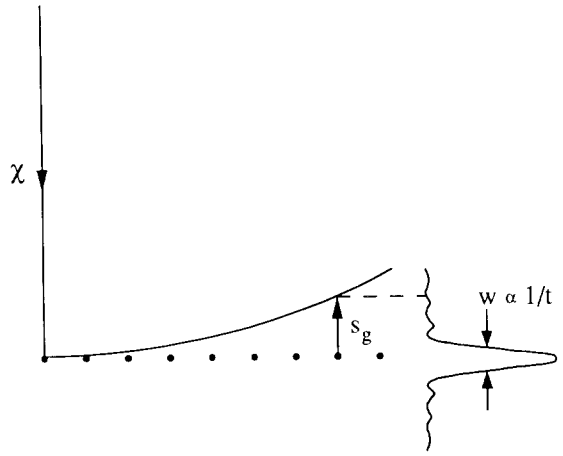

Fig. 3. Plot showing how the Ewald sphere intersects only the tails of high-order zero-layer reflections.

transverse incoherence with no contrast reversals, provided the beams reaching the detector are not highly dynamical. Contributions along the column do, however, add coherently to remove intensity from the detector. In reciprocal space this can be seen as simply the result of the shape factor (fig. 3). Due to the curvature of the Ewald sphere, it intersects only the tails of the high-order reflections. As the crystal thickness (t) is increased, the width (w) of the distribution decreases resulting in an oscillatory thickness dependence. The period of $8\pi\chi/g_1^2$ corresponds to a phase shift of 2π between electrons scattered from the top and bottom of the column. For a 75 mrad inner detector angle this corresponds to a periodicity of 26 Å. The coherently scattered high-angle intensity therefore never rises above that scattered by a very thin crystal, and we can therefore write a modified Treacy criterion appropriate for zone axis conditions by including the effect of the shape factor, giving

$$\frac{I^{\mathrm{HA}}}{I^{\text{zero layer}}} \approx \frac{\mathrm{e}^{-2M_\kappa s^2}\sin^2(\pi s_g t)}{(1-\mathrm{e}^{-2M_\kappa s^2})\pi^2 s_g^2 t} \lesssim 0.02, \qquad (11)$$

where s_g is the deviation parameter. For Si at room temperature, this condition is reached for a 75–150 mrad detector by a thickness of 50 Å.

Only with very thin crystals or thin overlayers of a heavy material on a light substrate will the coherent contribution be significant at these high detector angles. If the detector angles are reduced, then again the coherent component becomes more important and also more complicated as dynamical beams begin to reach the detector. In these cases a multislice approach is useful for image simulation [41,42]. We note that the high-angle thermal diffuse component could also be simply included in such a program by invoking the validity of the Einstein model described earlier, and simply summing the intensities at the atom sites scaled by the appropriate high-angle cross section (eq. (10)) for each successive slice. This would be very much more accurate than a single phonon low-angle approximation [16,17] and very much simpler than attempting to simulate the diffuse scattering through an ensemble of frozen phonons [43]. Care should be taken in the treatment of absorption somewhat, since the intensity at the atom sites is very strongly affected and is often not included in low-angle approximate treatments. Such a program would be valuable in ascertaining the effects of defects, surface relaxation, and other such phenomena which destroy the simple integration over thickness which we shall use in the next section to describe the imaging of perfect crystals.

It is also worth pointing out that the approach we describe here is exactly the same as had been used previously for discussion of channeling effects [44–46] and the production of secondary radiations such as X-ray emission [47–50] and cathodoluminescence [51]. Although previous treatments have been concerned with integrated signals, our description of high-resolution imaging in the next section applies equally well to these other signals, if they are localized to the region of the atomic cores. In principle, therefore, an atomic-resolution X-ray or electron-energy-loss image could be obtained, although in the electron case a collection angle sufficiently large to average over dynamical effects would be required. Also, since the detected signals are typically reduced by a factor of 10^4 to 10^6 compared to high-angle elastically scattered electrons it seems unlikely such images could be obtained with reasonable statistics. By using the high-angle annular detector to locate the probe over an atomic column it should be possible, however, to collect and interpret spec-

tra on a column-by-column basis, providing an exciting extension for high-resolution techniques.

3. The approach to incoherent imaging

The definition of incoherent imaging is that an object be illuminated incoherently or that it spontaneously emit radiation in an incoherent manner. The validity of the Einstein model at high angles means that the atoms do, in effect, scatter incoherently, and so we only need to consider the dynamical diffraction of the probe as it propagates through the crystal. Consider the case of the phase object familiar from coherent imaging theory, which exhibits sufficiently weak projected potential components that its effect on the incident wave function can be represented as multiplication by a phase factor. A phase object could comprise either a very thin crystal in a zone axis orientation or a much thicker crystal oriented far from any strong Bragg reflections. The probe intensity profile is unaltered by such an object, and since the high-angle signal is independent of the phase of the wave function we would see a true incoherent image as the probe was scanned across the crystal. Atomic columns would be resolved if the probe intensity profile were sufficiently narrow and the image would be given on incoherent imaging theory as a convolution,

$$I^{\mathrm{HA}}(\boldsymbol{R}) = O(\boldsymbol{R}) * P(\boldsymbol{R}). \tag{12}$$

Here, $O(\boldsymbol{R}) = \sum_i \sigma_i \delta(\boldsymbol{R} - \boldsymbol{R}_i)$, where $\sigma_i^{\varepsilon} = \sum_{\kappa} \sigma_{\kappa}$ represents the high-angle scattering power of atomic column i at position $\boldsymbol{R}_i$ and $P(\boldsymbol{R})$ is the probe intensity profile. In this thickness regime we would, of course, need to go to rather higher angles to avoid the coherent component (see eq. (11)).

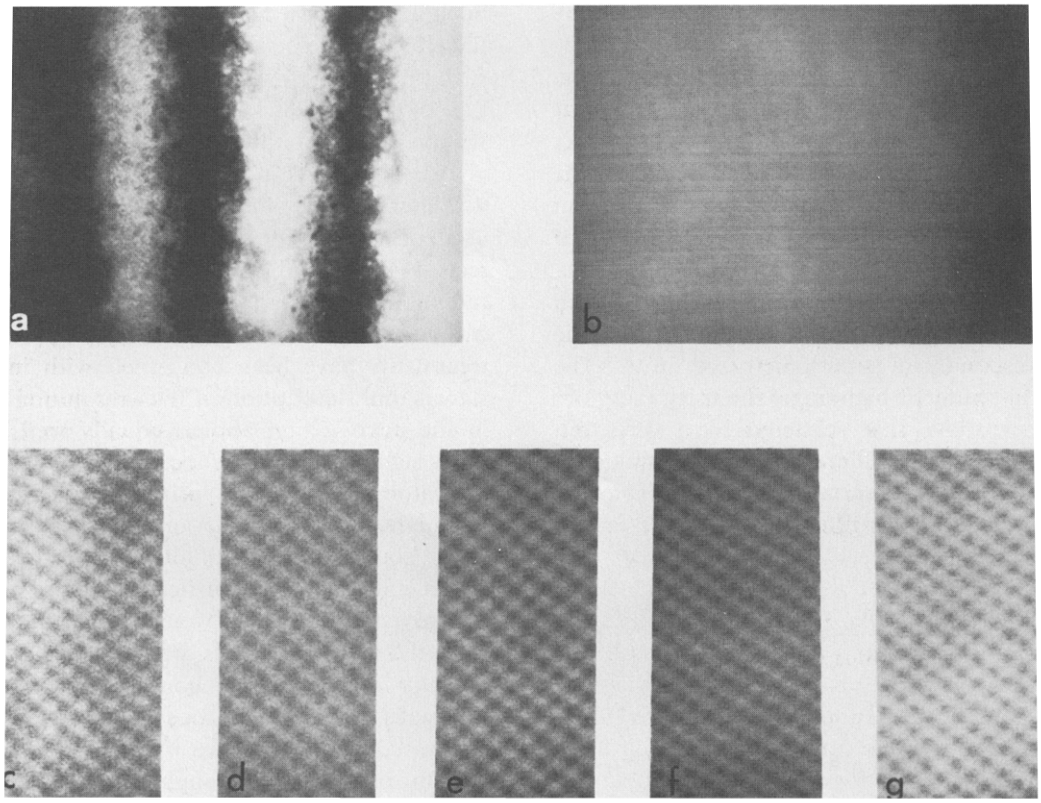

Fig. 4. Si⟨110⟩ imaged axially using a 10 mrad objective aperture to exclude the {111} beams. (a) Bright field. (b) High-angle annular detector image. (c–g) High magnification of (b) at thicknesses of 120, 230, 350, 470, and 610 Å, respectively.

Now the question arises as to the effect of the dynamical diffraction which the probe undergoes as it propagates deeper into the crystal. Experimentally, we find that there is practically no effect. Fig. 4 shows images from Si⟨110⟩ obtained using an objective aperture which just excluded the {111} beams. There is therefore no bright field phase contrast image (no overlapping discs reach the bright field detector) but instead a series of thickness fringes which can conveniently be used to measure sample thickness. No oscillations are seen with the high-angle detector, the contrast increasing monotonically over this thickness regime. At each thickness a high-resolution image is present, even beyond the 600 Å shown. These images are similar in form and exhibit only one obvious focus condition, exactly as we would expect for incoherent imaging. In detail, the image contrast slowly reduces with increasing sample thickness although the form of the image remains the same.

We shall find that with a Bloch wave description of the probe propagation it becomes particularly simple to explain these observations and to identify how closely we approach ideal incoherent imaging and an intuitively interpretable image [52]. The Bloch states represent the stationary states of the fast electron in the crystal (see, for example, Bird [35]). They take on the periodicity of the lattice in the transverse directions and propagate with slightly different wavevectors in the z direction. The power of the Bloch wave approach is that dynamical interaction of very many diffracted beams is described very well by the interference of just a few Bloch states. In our case we shall find that the problem simplifies to the extent that only a single Bloch state is important, which is the fundamental reason for the lack of any observable interference effects. For a plane wave incident on a crystal with transverse wavevector component $\boldsymbol{K}$ the wave function in the crystal $\psi(\boldsymbol{R}, z)$ is given by a sum of j Bloch states:

$$\psi(\boldsymbol{R}, z) = \sum_j \epsilon^j(\boldsymbol{K})\tau^j(\boldsymbol{R}, \boldsymbol{K})\, \mathrm{e}^{-\mathrm{i}s^j(\boldsymbol{K})z/2\chi}\, \mathrm{e}^{-\mu^j(\boldsymbol{K})z}, \tag{13}$$

where $\tau^j(\boldsymbol{R}, \boldsymbol{K}) = b^j(\boldsymbol{R}, \boldsymbol{K})\, \mathrm{e}^{\mathrm{i}\boldsymbol{K}\cdot\boldsymbol{R}}$ are the two-dimensional Bloch states of transverse energy $s^j(\boldsymbol{K})$, absorption $\mu^j(\boldsymbol{K})$ and excitation coefficients $\epsilon^j(\boldsymbol{K})$. For a coherent probe located at $\boldsymbol{R}_0$ the total wave function becomes

$$\begin{aligned}\psi(\boldsymbol{R}-\boldsymbol{R}_0, z) &= \sum_j \int_{\text{probe}} \epsilon^j(\boldsymbol{K}) b^j(\boldsymbol{R}, \boldsymbol{K})\, \mathrm{e}^{-\mathrm{i}s^j(\boldsymbol{K})z/2\chi} \\ &\quad \times \mathrm{e}^{-\mu^j(\boldsymbol{K})z}\, \mathrm{e}^{\mathrm{i}\boldsymbol{K}\cdot(\boldsymbol{R}-\boldsymbol{R}_0)}\, \mathrm{e}^{\mathrm{i}\gamma(K)}\, \mathrm{d}\boldsymbol{K} \\ &= \sum_j A^j(\boldsymbol{R}-\boldsymbol{R}_0, z),\end{aligned} \tag{14}$$

where A^j represents the amplitude contribution from each Bloch state integrated over the incident probe and $\gamma(K)$ is the usual phase factor due to spherical aberration C_s and defocus Δf, given by

$$\gamma(K) = \frac{\Delta f K^2}{2\chi} + \frac{C_s K^4}{4\chi^3}. \tag{15}$$

Our image will depend on the probe amplitude contributions close to the atom strings $\boldsymbol{R}_i$. Fig. 5 shows the first six Bloch states in Si⟨110⟩ for axial illumination. We see that they are similar to a set of molecular orbitals [45,53] comprising bonding and antibonding (denoted by *) combinations of

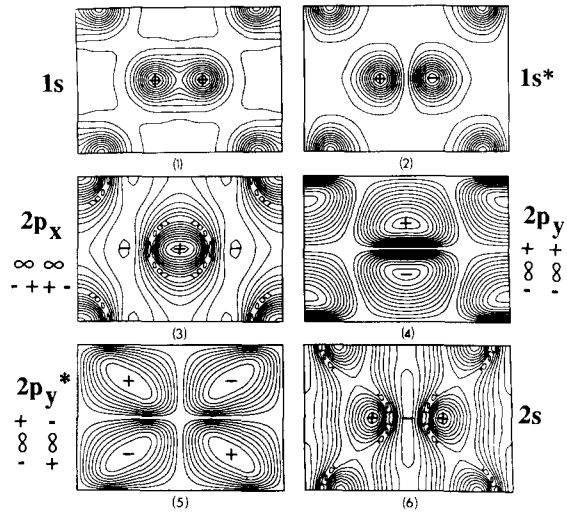

Fig. 5. The first six Bloch states for Si⟨110⟩ at 100 kV with their corresponding molecular orbital interpretations. Polarity is indicated by + or − signs.

s- and p-states, the s-states peaking near the atomic strings, the p-states having nodes near the strings. For a monatomic lattice, the peaks and nodes would lie exactly on the atom sites for axial illumination. For nonaxial illumination, this exact symmetry is broken and the p-states acquire some amplitude at the sites. However, now consider the effect of the coherent angular integration. Tightly bound s-states are relatively non-dispersive so that the amplitude contributions from the entire aperture disc add coherently to give a very large contribution. This does not happen with the more dispersive states. Their contribution to the amplitude at the atom sites, already small, does not add in phase over the aperture disc, so that we would expect the integrated intensity at the atom sites to be dominated by the s-state contribution. This behavior can be predicted by inspecting the form of the Bloch states and the dispersion surface. For the two-string Si case, shown in fig. 6, tightly bound s-states (1) and (2) (with respect to the zero transverse energy) are almost flat, while the other states are significantly more dispersive. Then eq. (9) for the image intensity can be written as

$$
\begin{aligned}
I^{\mathrm{HA}}(\boldsymbol{R}_0, t) &= \sum_i \sigma_i \int_0^t \Big[A^{1s^2}(\boldsymbol{R}_i - \boldsymbol{R}_0, z) \\
&+ A^{1s}(\boldsymbol{R}_i - \boldsymbol{R}_0, z) \sum_j A^j(\boldsymbol{R}_i - \boldsymbol{R}_0, z) \\
&+ \sum_j \sum_k A^j(\boldsymbol{R}_i - \boldsymbol{R}_0, z) A^k(\boldsymbol{R}_i - \boldsymbol{R}_0, z) \Big] \, \mathrm{d}z .
\end{aligned}
\tag{16}
$$

where we have treated the bonding and antibonding s-states (1) and (2) as a cluster due to their small separation in transverse energy [54]. The three intensity contributions in the square brackets can be recognized, respectively, as that due to the s-states alone, the cross terms between the s-states and all other states (dependent terms involving s-states), and finally the dependent ($j \neq k$) and independent ($j = k$) contributions from all states, where the sums over j and k exclude the s-states. Fig. 7 shows line traces calculated using all terms in eq. (16) (squares) and using only the independent s-state contribution (circles) both at 100 kV accelerating voltage and at 300 kV accelerating voltage, in which case the Si dumbbell is just resolved. Clearly the s-states are responsible

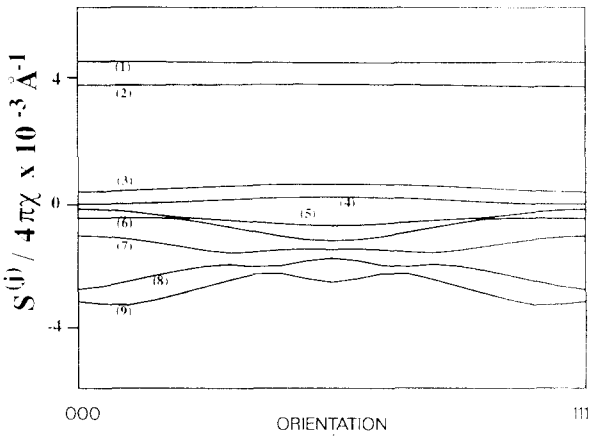

Fig. 6. Section of the dispersion surface for Si(110) at 100 kV.

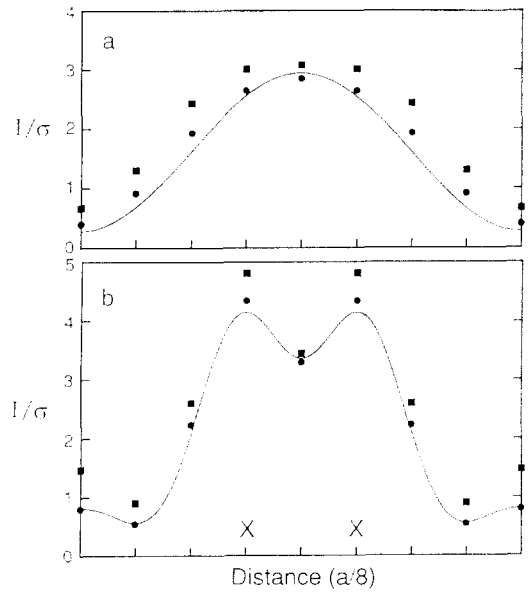

Fig. 7. Calculated image intensity across a Si[110] dumbbell from channel to channel along [001] through the atom sites X for accelerating voltages of (a) 100 kV and (b) 300 kV. The full dynamical result, eq. (16), is shown as squares, the s-state contribution alone as circles, and the effective probe approximation eq. (18) is shown as the solid line. Calculations assume optimum illumination angle $(4\lambda / C_s)^{1/4}$ and defocus $(C_s\lambda)^{1/2}$ for an objective lens $C_s = 1.3$ mm [52].

for practically the entire image contrast, the effect of all other states appearing as a uniform background in the image.

This is the key reason for the incoherent characteristics of the image. The high-angle detector is sensitive only to the intensity very close to the atomic sites, which is dominated by *s*-type Bloch states. The detector, therefore, acts as a very effective Bloch state filter with the result that interference effects are removed from the image. This behavior is in marked contrast to conventional imaging in which all states at the exit surface of the crystal contribute to the image, resulting in its very strong thickness dependence (see Kambe [55] for a Bloch wave description of this).

The coherent addition of the *s*-states coupled with the destructive interference of all other states explains several previous calculations of the probe propagation through crystals [56,42], in which it was noticed that the beam sharpened up around the atomic strings with a correspondingly low intensity between. For an incident probe covering many strings an array of strongly channeled intensity spikes was found having the incident probe profile as an envelope. These are all manifestations of exactly the same phenomenon. Our detector probes only that portion of the probe profile at the atomic strings which has a particularly simple, almost classical behavior. Channeling is not necessary for the image as noted previously, but it does result in a much increased image efficiency from the typical sample thicknesses employed for high-resolution microscopy.

To see how closely the image approaches ideal incoherent imaging let us examine the *s*-state contribution in more detail. From eqs. (14) and (16) we obtain

$$I^{\mathrm{HA}}(\boldsymbol{R}_0, t) \approx \sum_i \sigma_i^{\mathrm{c}} \int_0^t \left| \int_{\mathrm{probe}} \epsilon^{1\mathrm{s}}(\boldsymbol{K}) b^{1\mathrm{s}}(\boldsymbol{R}_i, \boldsymbol{K}) \times \mathrm{e}^{-s^{1\mathrm{s}}(\boldsymbol{K})z/2\chi} \, \mathrm{e}^{-\mu^{1\mathrm{s}}(\boldsymbol{K})} \, \mathrm{e}^{\mathrm{i}\boldsymbol{K}\cdot(\boldsymbol{R}_i - \boldsymbol{R}_0)} \times \mathrm{e}^{\mathrm{i}\gamma(K)} \, \mathrm{d}\boldsymbol{K} \right|^2 \mathrm{d}z. \quad (17)$$

Recall that the reason the *s*-states dominate the angular integration is that they are non-dispersive. Therefore, to a good approximation we can take them outside the angular integration to give

$$I^{\mathrm{HA}}(\boldsymbol{R}_0, t) \approx \sum_i \sigma_i^{\mathrm{c}} \int_0^t \left| \epsilon^{1\mathrm{s}}(0) b^{1\mathrm{s}}(\boldsymbol{R}_i, 0) \, \mathrm{e}^{-s^{1\mathrm{s}}(0)z/2\chi} \times \mathrm{e}^{-\mu^{1\mathrm{s}}(0)z} \right|^2 \mathrm{d}z \times \left| \frac{1}{\epsilon^{1\mathrm{s}}(0)} \int_{\mathrm{probe}} \epsilon^{1\mathrm{s}}(\boldsymbol{K}) \times \mathrm{e}^{\mathrm{i}[\boldsymbol{K}\cdot(\boldsymbol{R}_i - \boldsymbol{R}_0) + \gamma(K)]} \, \mathrm{d}\boldsymbol{K} \right|^2. \quad (18)$$

The thickness integration is now independent of the incident probe, and is therefore simply a property of the object. The second term involving the incident beam is independent of thickness, and if it were not for the angular variation in *s*-state excitation $\epsilon^{1\mathrm{s}}(\boldsymbol{K})$ it would be identically the incident probe intensity profile. The image is therefore given in this approximation as a simple convolution

$$I^{\mathrm{HA}}(\boldsymbol{R}_0, t) = O(\boldsymbol{R}_0, t) * P^{\mathrm{eff}}(\boldsymbol{R}_0), \quad (19)$$

where $O(\boldsymbol{R}_i, t)$ is the object function given by

$$O(\boldsymbol{R}_i, t) = \sum_i \sigma_i^{\mathrm{c}} \epsilon^{1\mathrm{s}^2}(0) b^{1\mathrm{s}^2}(\boldsymbol{R}_i, 0) \left(\frac{1 - \mathrm{e}^{-2\mu^{1\mathrm{s}}(0)t}}{2\mu^{1\mathrm{s}}(0)} \right) \quad (20)$$

and

$$P^{\mathrm{eff}}(\boldsymbol{R}) = \left| \frac{1}{\epsilon^{1\mathrm{s}}(0)} \int_{\mathrm{probe}} \epsilon^{1\mathrm{s}}(\boldsymbol{K}) \, \mathrm{e}^{\mathrm{i}\gamma(K)} \, \mathrm{d}\boldsymbol{K} \right|^2 \quad (21)$$

is an effective probe intensity profile. The incident probe for comparison is given by

$$P(\boldsymbol{R}_0) = \left| \int_{\mathrm{probe}} \mathrm{e}^{\mathrm{i}[\boldsymbol{K}\cdot(\boldsymbol{R} - \boldsymbol{R}_0) + \gamma(K)]} \, \mathrm{d}\boldsymbol{K} \right|^2. \quad (22)$$

The fall-off in *s*-state excitation $\epsilon(\boldsymbol{K})$ is quite slow, reaching a typical value of 0.6–0.8 $\epsilon(0)$ for Si⟨110⟩ at our aperture cut-off. Heavier strings with more tightly bound *s*-states fall off even more slowly. Multiplication in reciprocal space by this broad function is equivalent to convoluting the incident probe in real space by a very narrow

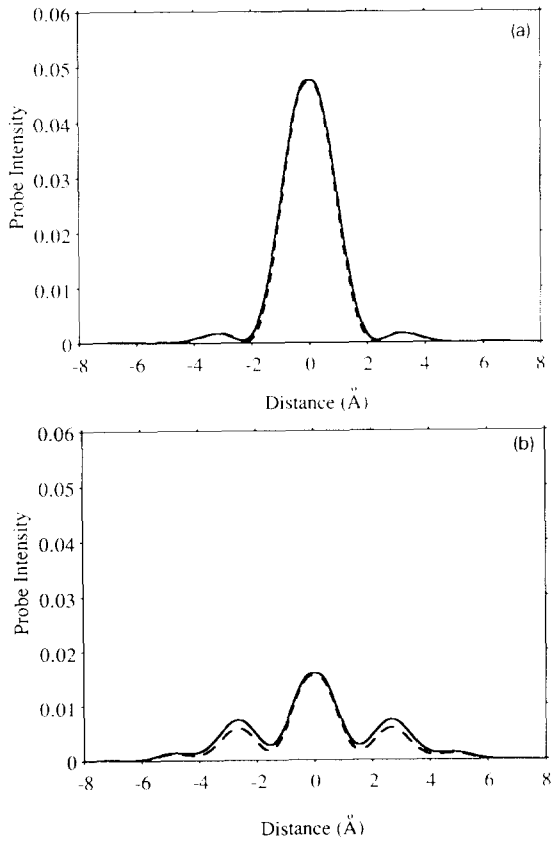

Fig. 8. Comparison of the effective probe (solid) and incident probe (dotted) intensity profiles for 100 kV accelerating voltage, objective lens $C_s = 1.3$ mm and defocus values of (a) -693 Å, (b) -1100 Å. The incident probe profile has been multiplied by a factor of 0.70 in (a) and 0.59 in (b).

function, with the result that the resolution of the image is little affected, as shown in fig. 8. For optimum focus, the effective probe profile is practically indistinguishable from the incident probe profile scaled by an appropriate factor $S(K_c)$ which at optimum focus is very close to

$$S(K_c) \approx \left[\int_{\text{probe}} \epsilon^{1s}(\boldsymbol{K})\, \mathrm{d}\boldsymbol{K}/\pi K_c^2 \epsilon^{1s}(0)\right]^2, \qquad (23)$$

where K_c is the aperture cutoff.

All the remaining materials-dependent terms are contained in the object function which consists of an array of δ-functions located at the atomic strings with a strength given by the thickness-integrated s-state intensity at the atom sites weighted by the screened high-angle cross section. The thickness dependence would be linear if it were not for the absorption term, which gradually reduces the intensity at the sites with increasing depth so that eventually no further contribution to the image occurs. Saturation occurs more quickly with stronger absorption, in Ge compared to Si, for example, as shown in fig. 9. Also shown in fig. 9 are the results of the fully dependent calculation, eq. (16), which differ little above 100 Å although more significantly in thin crystals. The oscillatory behavior in the thin-crystal regime represents the dependent cross term between the s-state cluster and a cluster comprising states close to the tops of the potential wells. With increasing thickness the other states resolve individually and the cross

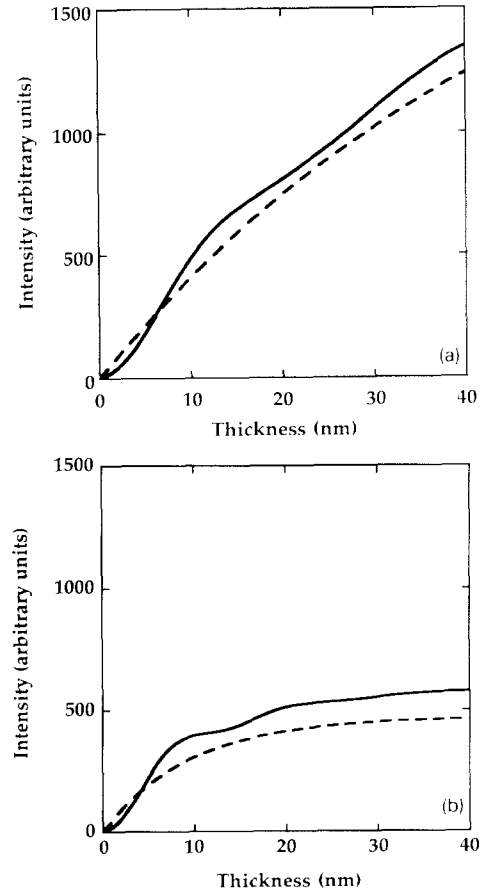

Fig. 9. Thickness dependence of the object function in (a) Si⟨110⟩ and (b) Ge⟨110⟩ calculated using the full dependent calculation (solid lines) and using the s states alone (dotted lines).

terms become progressively less important compared with the independent contributions of the various states. The offset at larger thickness probably indicates a small non-dispersive contribution from the 2s state. Note that there is also some evidence to suggest that the absorption coefficients may be too high when calculated by integrating over the entire reflecting sphere. The *s*-state absorption is quite localized and will show an incoherent image itself, which should be added to the basic image. This contribution will be quite weak, however, since most absorbed electrons will not be propagating in strongly channeling directions, and would tend to sense the average material composition. We see also that no beam broadening effects can occur. The resolution is set by the probe profile at the entrance surface to the crystal. With increasing thickness the *s*-states become absorbed while the background intensity resulting from all other states increases, so that we expect the image contrast to reduce but the resolution to be unaffected, which is in agreement with experimental observations.

We see then that the image does, to a very good approximation, represent the ideal incoherent imaging of a crystal in the form of an object function $O(\boldsymbol{R})$ convoluted with a resolution function $P^{\text{eff}}(\boldsymbol{R})$. For optimum focus, $P^{\text{eff}}(\boldsymbol{R})$ is very similar in form to $P(\boldsymbol{R})$, the incident probe intensity profile, so that we see the expected improvement in resolution compared to coherent bright-field imaging based on the amplitude profile. It is also clear that with only one dominant Bloch state we can have no contrast reversals with sample thickness. Even if several significantly excited *s*-states are non-dispersive, as may occur with stronger strings, this will only introduce a modulation to the thickness dependence of the object function.

It is a simple matter to extend these ideas to more complicated structures consisting of different types and arrangements of strings. The object function now consists of an array of δ-functions with different strengths for different strings (in general), each constructed from their individual s-state parameters according to eq. (20). Differences in the s-state excitation $\epsilon(\boldsymbol{K})$ can be incorporated into the object function through the scaling factor $S(K_c)$, and the new object function would then be convoluted with the incident probe. Due to absorption, the relative contrast between different string types will be dependent on sample thickness and is quite predictable from the object function. In principle, it would seem possible for a compositional reversal to occur, the higher absorption for a higher Z string giving less integrated intensity than a lighter, less absorbing string, although we have yet to see an example of this. It appears that differences in absorption are sufficiently small compared to differences in the cross sections that the image is lost into the background before a reversal can occur.

If the string separations are large compared with the spatial extent of the *s*-states, then the strength of the strings will approximate those of the isolated strings. In this case more complicated unit cells, interfaces, and superlattices can be constructed by assembling an appropriate array of isolated string strengths without the need for supercell Bloch state calculations. This, of course, breaks down for closely spaced identical strings such as the Si dumbbell considered here where the *s*-states overlap, but this can be easily handled by choosing appropriate molecular orbital states. Even in the Si case the difference from the isolated string case is less than 10% [57], and the problem is unlikely to arise if the Bloch states have different transverse energies as is generally true for different string types. The tightly bound *s*-states are relatively insensitive, therefore, to the distribution and strength of surrounding strings, or randomly distributed atoms, so that images from interfaces show no interference or Fresnel fringe effects, another characteristic of incoherent imaging (see fig. 10). Again, this contrasts markedly to the situation for coherent imaging in which weakly bound states sampling the regions in between the strings can have a strong effect on the image. In this case the image of a string will be very sensitive to the nature and arrangement of surrounding strings, which is why conventional images of defects, interfaces, and superlattices must be simulated as individual objects in their own right.

With Z-contrast imaging the vast majority of samples can be described through the object func-

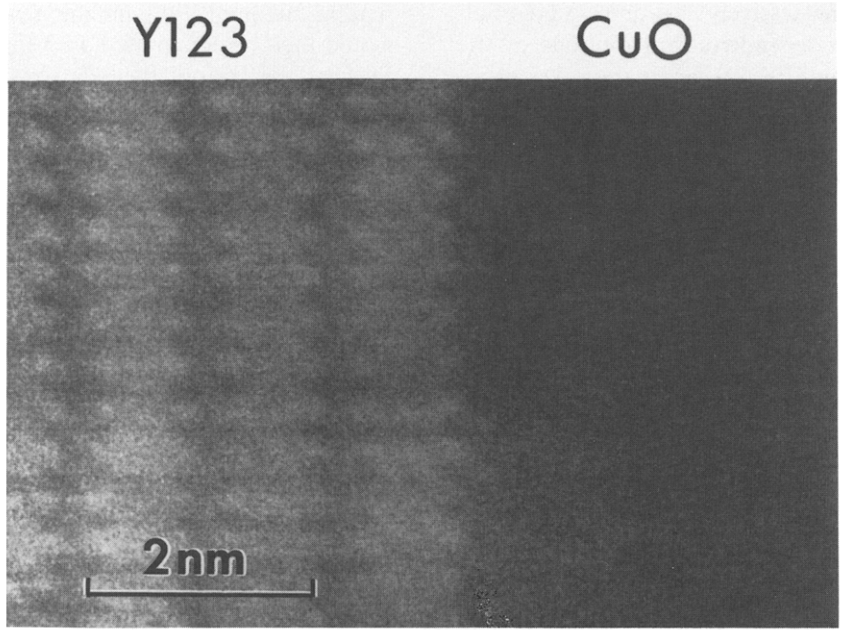

Fig. 10. Boundary between a grain of $YBa_2Cu_3O_{7-\delta}$ viewed along the a (or b) axis and a CuO precipitate viewed in a random orientation. The bright Ba columns dominate the image, the Y columns being less clear in between, while the Cu oxide columns are unresolved. No Fresnel fringe effects obscure the boundary which is clearly located after the Ba plane.

tion approach with huge savings in computer time. Indeed it is particularly simple to visualize the object function, since all strings will have s-states, each string will contribute a δ-function with a strength determined predominantly by the high-angle cross section. The variations with thickness and s-state parameters tend to be second order, although they are simple to calculate, so that the approximate form of the object function is intuitively predictable for any crystal structure. In the next section we consider the optimum conditions for imaging such an object.

We should also point out that the Bloch states are generally expressed (including in our calculations to date) in terms of their plane wave expansions

$$\tau^j(\boldsymbol{R}, \boldsymbol{K}) = \sum_{\boldsymbol{G}} C_{\boldsymbol{G}}^j \, e^{i(\boldsymbol{K}+\boldsymbol{G})\cdot\boldsymbol{R}}, \tag{24}$$

where $\boldsymbol{G}$ are the zero-layer reciprocal lattice vectors. For accurate determination of the amplitudes of highly localized states at the atom sites these series converge rather slowly, particularly for large unit cells, and therefore become computationally inefficient. In conventional diffraction or phase contrast calculations the diffracted beam amplitudes at the exit surface are required for calculating the image, but in our case we need only consider the Bloch state amplitudes themselves. More efficient methods for calculating tightly bound Bloch states therefore become appealing [45,58,59].

4. Choice of optimum probe

The crystal has now in effect been replaced by an array of δ-functions at the atomic string positions and we need to consider the most suitable imaging probe. We must distinguish at the outset between image resolution and compositional resolution. Image resolution is normally defined in terms of a two-point Rayleigh criterion, a simple visual condition for recognizing that the object consists of two scattering centers. By compositional resolution we mean determining the relative columnar scattering strengths, which is a significantly more stringent condition. If we are to de-

termine the relative strengths of two adjacent columns from the image alone with no prior knowledge, then obviously the two columns must be sufficiently spatially separated so that a probe centered on one has negligible intensity on the other, in which case we can say we have column-by-column imaging conditions. Let us first consider the Rayleigh criterion for two point scatterers. In light optics we know that resolution is limited primarily by diffraction and the Rayleigh resolution limit is defined as the radius of the first zero of the Airy disc intensity profile, which for a circular aperture occurs at $0.61\lambda/\alpha$. Two point sources with this separation show a clear dip between the maxima (to 73.5% of the peak intensity) and the objects are said to be resolved [60]. In the electron case, spherical aberration is severe and increases rapidly with increasing aperture size with the result that there exists an optimum aperture α_{opt} and an optimum defocus Δf_{opt}, where the two aberrations balance to produce a minimum probe size. This problem was first analyzed by Scherzer [61], who arrived at the conditions

$$\alpha_{opt} = (4\lambda/C_s)^{1/4}, \tag{25}$$

$$\Delta f_{opt} = -(C_s\lambda)^{1/2}, \tag{26}$$

under which the probe intensity profile is very similar to the Airy disc so that the resolution limit is defined again as

$$d_{min} = 0.61\lambda/\alpha_{opt} = 0.43C_s^{1/4}\lambda^{3/4}. \tag{27}$$

These are also the conditions adopted by Crewe and coworkers [5,62]. d_{min} is very close to the position of the first intensity minimum and to the FWHM of the central peak. We refer to these conditions as the Scherzer incoherent conditions to distinguish them from his more familiar phase contrast conditions ($d_{min} = \lambda/\alpha_{opt} = 0.66 C_s^{1/4}\lambda^{3/4}$, see also Cowley [63]). We see the usual improvement in resolution associated with incoherent imaging, although both with coherent and incoherent imaging the resolution may be pushed beyond the Scherzer limit by the use of other imaging conditions, usually accompanied, however, with a loss of interpretability.

Fig. 11 shows an array of probes for various values of α and Δf, the central one corresponding

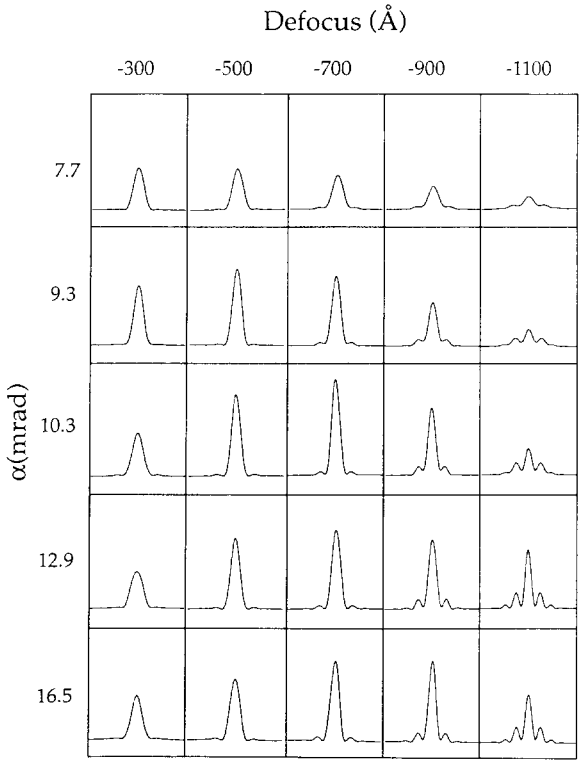

Fig. 11. Effective probe intensity profiles for various objective aperture semiangles α and defocus values calculated for Si⟨110⟩ at 100 kV accelerating voltage and $C_s = 1.3$ mm. The full width of each profile is 20 Å.

to the Scherzer incoherent conditions, and fig. 12 the corresponding image simulations for Si⟨110⟩. To afford direct comparison, fig. 11 shows damped probes appropriate for Si⟨110⟩ calculated with eq. (21). The smaller values of α and Δf result in diffraction-limited probes with broad central maxima and very weak tails, whereas larger values of α and Δf result in more extended tails although the probes have a narrower central peak. The tails are responsible for the haloes around the atomic columns on the right-hand images, which is an example of false detail. The Scherzer optimum conditions do seem to give the "best" overall image, and it is also clear that a defocus sequence shows no reversals. In general it seems that the introduction of false detail at higher defocus values is accompanied by a substantial loss of image contrast and would not be mistaken experimentally for the optimum condition.

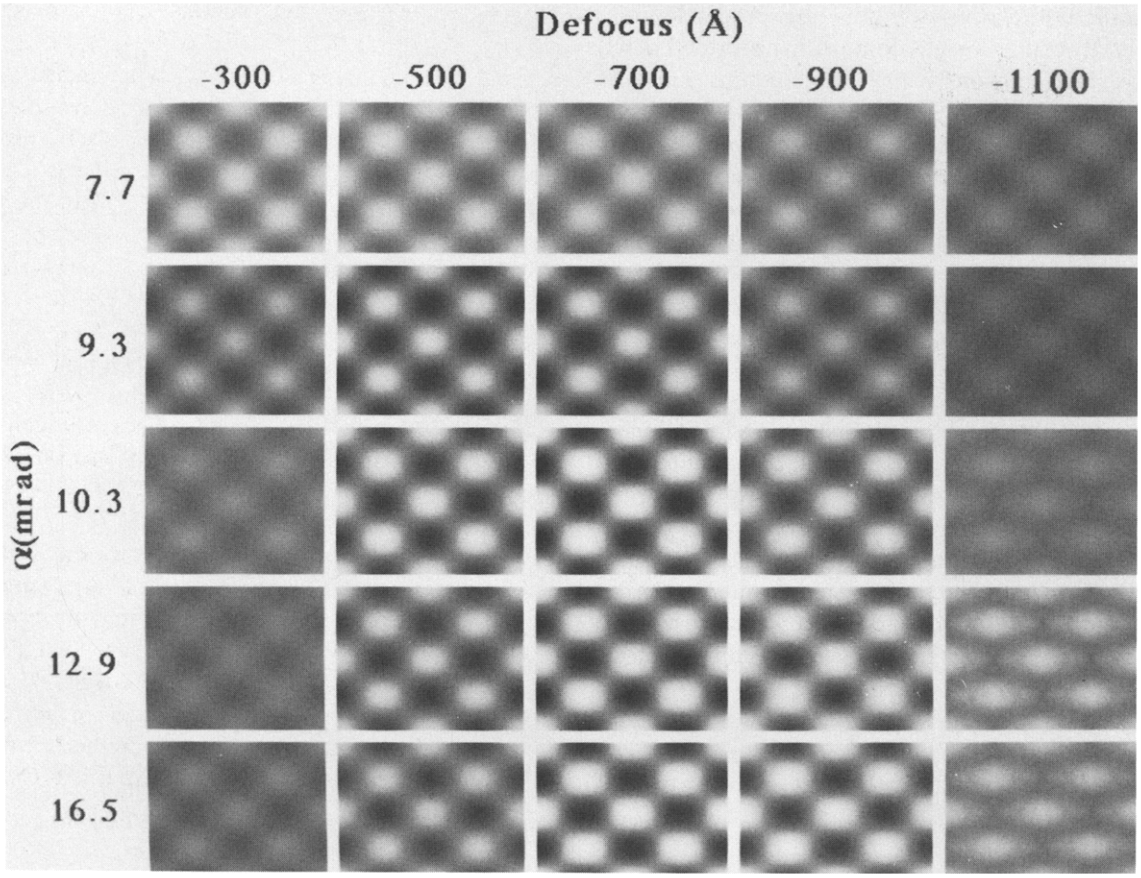

Fig. 12. Simulated images of Si⟨110⟩ corresponding to the probes shown in fig. 11.

A different optimization procedure has been discussed by Mory et al. [64] for the situation where the object is continuous rather than discrete, for example, as occurs in microanalysis with random crystal orientations. Instead of minimizing the probe intensity profile itself, in this case it is necessary to minimize the width of $P(R)\,2\pi R$, which is the integrated intensity in an annulus at radius R. This increases the relative contributions of the tail regions and results in the optimum conditions $\alpha_{opt} = 1.27(\lambda/C_s)^{1/4}$ and $\Delta f_{opt} = -0.75(C_s\lambda)^{1/2}$ giving $d_{min} = 0.48C_s^{1/4}\lambda^{3/4}$ using the definition of $d_{min} = \lambda/\alpha_{opt}$ (note that Mory et al. adopt a more stringent resolution criterion). These conditions correspond to $\alpha = 9.3$ mrad and $\Delta f = 520$ Å and give a good image though with somewhat less contrast than the Scherzer condition (fig. 12). The probe width is slightly larger to allow the tails to be reduced, so that the resolution is sacrificed somewhat to gain localization of the integrated current density. In practice our imaging falls somewhere in between the two-point Rayleigh criterion and the annular integration criterion since a probe centered on one dumbbell sees 4 neighboring strings at a radius of 2.80 Å and 8 at a radius of 3.90 Å. For a precise definition of resolution we would therefore need to define different optimum conditions for each object. Since the Scherzer and Mory conditions differ rather little in practice it would seem more appropriate simply to adopt the original Scherzer conditions.

It is, of course, also possible to go the other way and improve the image resolution by narrowing the central maximum, at the cost of reduced

image localization due to larger probe tails. For example, at $\alpha = 16.5$ mrad and $\Delta f = 900$ Å the first minimum occurs at just below 2 Å (see fig. 1) and experimental images have, in fact, demonstrated a resolution of below 2 Å at 100 kV accelerating voltage [38,39]. The price paid for this is less image localization, i.e., poorer compositional resolution. With the 2 Å probe above centered over one Si dumbbell only 72% of the image intensity comes from that dumbbell, the remainder coming from the surrounding dumbbells illuminated by the tails of the probe. For the Scherzer incoherent condition, the localization improves to 84% and still further to 93% for the Mory probe. Thus, we see a clear trade-off between image resolution and image localization, or compositional resolution.

Fig. 13 illustrates this point for Si_6Ge_6 and Si_2Ge_2 superlattices imaged with the Scherzer optimum probe and the higher resolution probe. Although the simulations look similar at first sight, the right-hand simulations clearly show the expected compositional blurring due to the tails of the high-resolution probe. In the case of Si_6Ge_6 superlattice with the probe centered over a dumbbell of Si or Ge at an interface, two of the six surrounding dumbbells are the other composition, with the result that the Si dumbbell appears more intense and the Ge dumbbell less intense than a corresponding dumbbell away from the interface. Such effects could be mistaken for real compositional variations although they can be easily predicted from the probe profile and reflect the result of the convolution as opposed to any change in the object function itself. A similar compositional blurring has been noticed in multislice calculations of a Si/Ge interface using a probe with extended tails [16,17]. These are practically absent in the left-hand simulation of fig. 13, and such an image represents a column-by-column compositional map where changes in intensity can be related directly to changes in column composition to an accuracy of around 10% [57].

The Scherzer optimum conditions would, therefore, seem to represent a good compromise between image contrast and image localization. Attempts to push beyond the Scherzer limit will suffer significantly from compositional blurring, although image simulation can still be performed accurately by the convolution method. Imaging becomes nonintuitive only because it is difficult to visualize the effects of the convolution with a

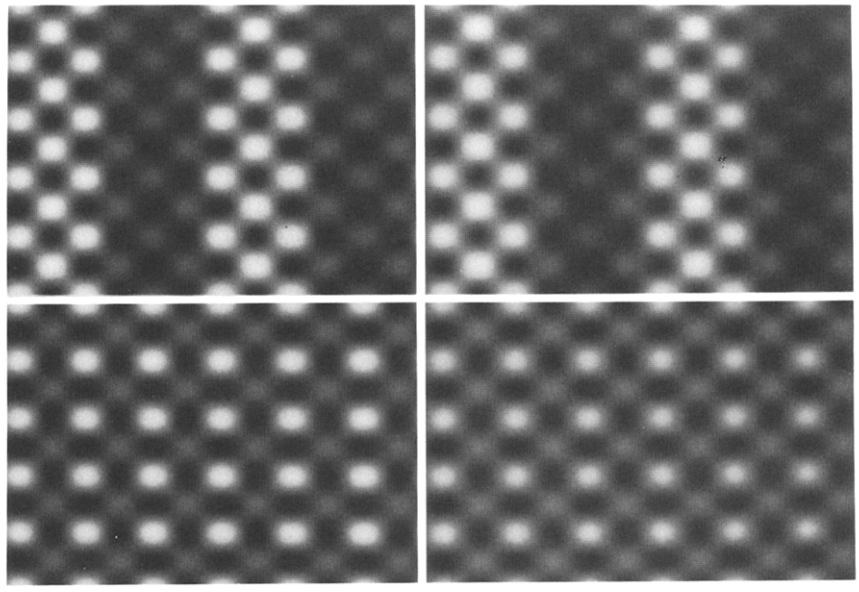

Fig. 13. Simulated images of Si_6Ge_6 (upper) and Si_2Ge_2 (lower) superlattices viewed along ⟨110⟩ for the Scherzer optimum probe (left), and a high-resolution probe $\alpha = 16.5$ mrad, $\Delta f = -900$ Å (right) showing compositional blurring due to probe tails.

probe having extended tails. With a Scherzer optimum probe it is relatively simple to visualize the convolution, even for column separations well below d_{min} as shown in the next section. Compositional mapping represents the most stringent criterion, and column separations 50% greater than d_{min} are really needed for a unique and intuitive assignment of column compositions.

5. Examples of incoherent Z-contrast imaging

One of the most useful aspects of the technique is that for a Scherzer optimum probe the form of the image is intuitively predictable simply from the form of the crystal projection even on a scale below the resolution limit. This is already apparent from the experimental and simulated images of Si⟨110⟩ (figs. 4 and 12, respectively). The 1.36 Å separation between the two columns comprising the dumbbell is well below the 2.2 Å resolution limit, and so the columns are unresolved. The image of the dumbbell is, however, clearly elongated along the ⟨100⟩ direction as expected, showing how information below the resolution limit is still contained in the image in a predictable and simply interpretable fashion. Indeed, if we did not know the crystal structure, the observation of the elongated image features would demonstrate the presence of two (or more) strings. Since the strings are replaced by δ-functions in the object function, with a correctly stigmated probe and axial incidence the only possible cause of an elongated image feature would be spatially separated scattering centers. The limit to which such information can be extracted is set by the statistics of the image and the accuracy of the convolution approximation, and it seems entirely feasible from our present results to extract information at least down to a level of $d_{min}/2$.

In fig. 14 we present an image of the ordered phase of Ni_3Al [65]. Again the general form of the image is predictable without any image simulation. The 1.78 Å separation of the Ni columns is below our resolution limit, and the individual strings are unresolved. However, due to the strong Z dependence of the high-angle scattering cross sections the Al column is imaged dark, resulting in

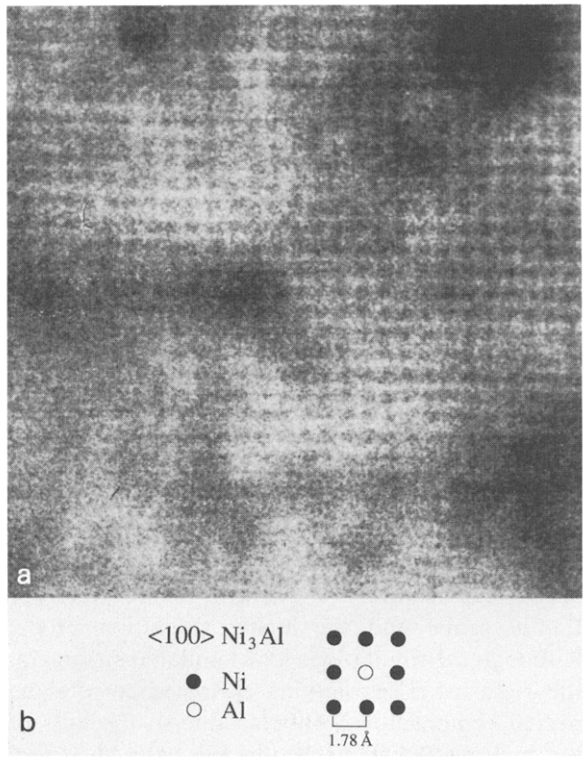

Fig. 14. Z-contrast image of (100) Ni_3Al showing a boundary between a grain of the ordered alloy and an epitaxial but disordered grain boundary phase. The schematic shows the arrangement of strings in the ordered phase.

the "basket-weave" form of the image. Here the contrast is entirely due to the compositional sensitivity since all nearest-neighbor column separations are below the resolution limit. In the lower part of the figure a disordered Ni-rich phase in the same orientation shows no image contrast.

Fig. 15 shows an image of a nominally 5.66 Å GaAs quantum well between $In_{0.5}Ga_{0.5}P$ barrier layers [66]. The GaAs shows bright, as expected considering the various cross sections (and even by approximating the cross section by Z^2). It clearly demonstrates a compositionally abrupt interface, although an interface step can also be seen. Closer inspection reveals image features with different shapes. The light P string contributes negligibly to the image so that the $In_{0.5}Ga_{0.5}P$ images as a lattice of circular features located over the In strings. GaAs images as elongated dumb-

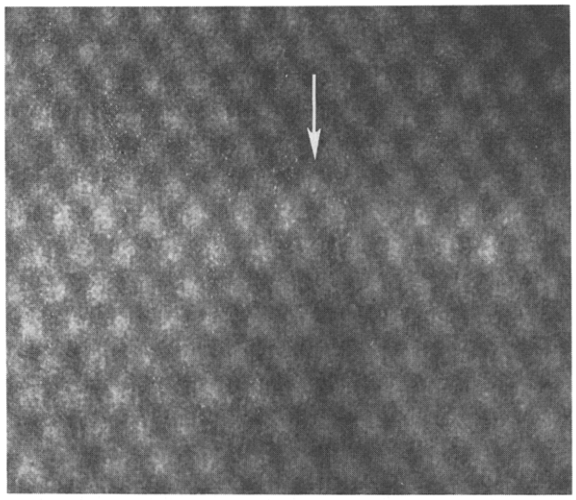

Fig. 15. Z-contrast image of a GaAs quantum well nominally a single unit cell thick between $In_{0.5}Ga_{0.5}P$ barriers. An interface step is arrowed.

bells since there is little difference between the cross sections of Ga and As. There will, therefore, be a relative shift of $\frac{1}{8}a\langle 100\rangle$ between the images of GaAs dumbbells and $In_{0.5}Ga_{0.5}P$ dumbbells which could be used to determine the polarity of the lattice. If we also allow the interface to be located within an individual dumbbell we have four possible configurations of the interface. By careful analysis of such images it should be possible to determine not only the compositional abruptness but the precise interface chemistry and the nature of the interface steps along the quantum well [67]. It is information of this kind which is required for correlating the optical properties of these devices with growth conditions.

It is important to realize that all these images were obtained with the same (optimum) probe conditions. In phase contrast imaging different structures will have different optimum values of objective aperture, defocus, and sample thickness so that effects which were not anticipated originally can easily be missed. With the Z-contrast technique any unexpected structures will be immediately apparent. Fig. 16 shows a striking example of such an effect at an interface between epitaxial $CoSi_2$ and Si(100) grown by a template method [68]. Generally assumed to be atomically flat over extended regions, here the interface is clearly stepped in an almost periodic fashion. The Z-contrast image of the $CoSi_2$ highlights the Co columns which show an apparent 4×1 compositional ordering at the interface plane, although this periodicity does not cover extended regions (an antiphase boundary can be seen in the figure) and does not show up in diffraction studies [69]. It seems most likely, therefore, that rather than representing an intrinsic interface reconstruction these structures represent interface defects. It is well

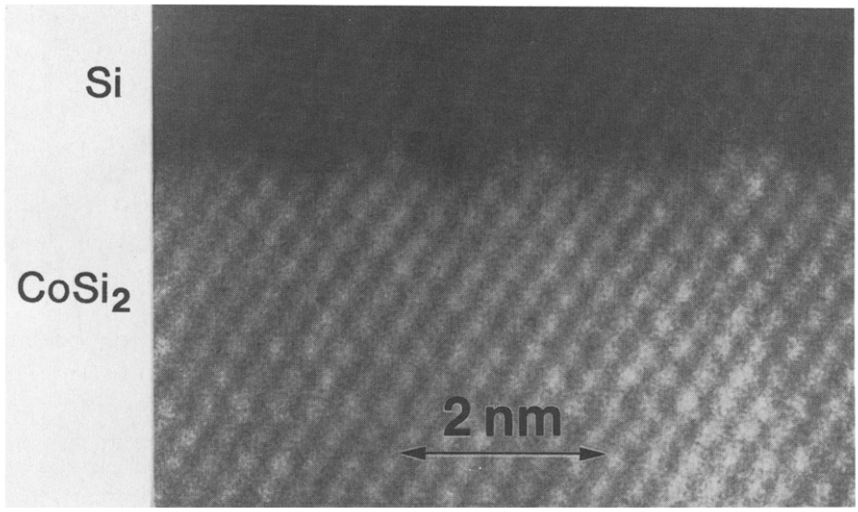

Fig. 16. Imaging of interfacial defects at an epitaxial $CoSi_2$/Si(100) interface.

known from scanning tunneling microscopy that various defects are present on the original Si surface after cleaning [70,71], and they could well be preserved during reaction of Co with the first few monolayers of Si to form the template layer. The electrical properties of such defects are entirely unknown and could well be affecting or even determining the measured Schottky barrier height.

Another example of an unexpected ordering effect is shown in fig. 17, which shows a region of an ultrathin Si_4Ge_8 superlattice grown on Ge(100) [72]. Ordering is seen within the narrow Si layers, alternate {111} planes showing brighter indicating the presence of Ge in an ordered phase. Notice that the compositional ordering is out of phase in the two neighboring Si layers. Although at first sight this would appear to be the ordered phase proposed by Littlewood [73], other areas show very different forms of ordering involving a reversal or a termination of the ordering. We also observe an asymmetrical interfacial abruptness, the interface at which Si was deposited onto Ge showing both a higher Ge content and a more extended ordered structure than the other interface. None of these phases correspond to the simple ordered forms previously proposed [73–76] and involve ordering on two sets of {111} planes simultaneously. The ordering is extinguished in each Ge layer and usually a different phase starts in each successive Si layer. The fact that the same phase is observed (though displaced) in fig. 17 is statistical chance. All these phases and the asymmetry of the compositional profiles can be explained by a rather simple Ge atom pump mechanism [77]. This involves interchange of a Ge adatom with an underlying Si atom at the rebonded edge configuration, which appears alternately during monolayer step growth on a (2×1) reconstructed surface [78]. *Z*-contrast imaging therefore provides appreciable insight into the atomistic details of the growth process itself.

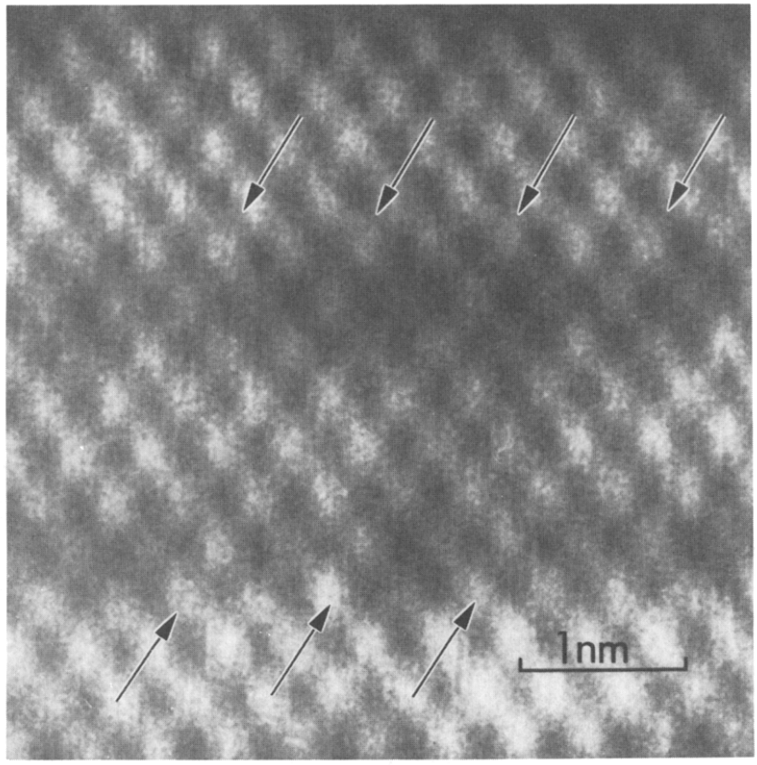

Fig. 17. Part of a Si_4Ge_8 ultrathin superlattice showing the presence of Ge within the Si layer in an ordered form (arrowed).

Currently, there is much interest in the growth of superlattices involving the oxide superconductors, for example $YBa_2Cu_3O_{7-x}/PrBa_2Cu_3O_{7-x}$ superlattices in which the $PrBa_2Cu_3O_{7-x}$ is insulating, with the aim of investigating the fundamental physics of superconductivity in these materials, for example, interlayer coupling and flux pinning. Obviously the compositional state of the interface is a key question, particularly since the alloy $Y_yPr_{1-y}Ba_2Cu_3O_{7-x}$ shows a great reduction in T_c with increasing Pr content. Fig. 18 shows part of such a superlattice grown by laser ablation [79] and it is immediately clear that no significant interdiffusion has occurred. The interface step in fig. 18b indicates a compositional abruptness even within the (horizontal) a–b plane of the order of a single lattice spacing. Since diffusion within the a–b plane is expected to be significantly higher than diffusion along the c axis this is further confirmation of the lack of any significant interdiffusion in the c direction. It is also clear that the compositional modulation is not quite parallel to the crystallographic c axis and in addition is somewhat wavy. This means that techniques which analyze an extended region, such as observation of satellite peaks in X-ray diffraction, would lead one to believe that interdiffusion had occurred on the scale of a few unit cells, which would, of course, explain the greatly reduced T_c values observed in the superlattices comprising single and double unit cell $YBa_2Cu_3O_{7-x}$ layers. This explanation is ruled out by the Z-contrast image, although one must now consider the effects of the waviness. This forces the current to cross from cell to cell and may greatly increase the density of pinning sites or the density of weak links compared with a thick film. The Z-contrast image again provides great insight into the growth process itself, since fig. 18 can only be explained if growth proceeds by an island growth mechanism where the height of the island is the full c-axis unit cell itself. Thus, the laser ablation

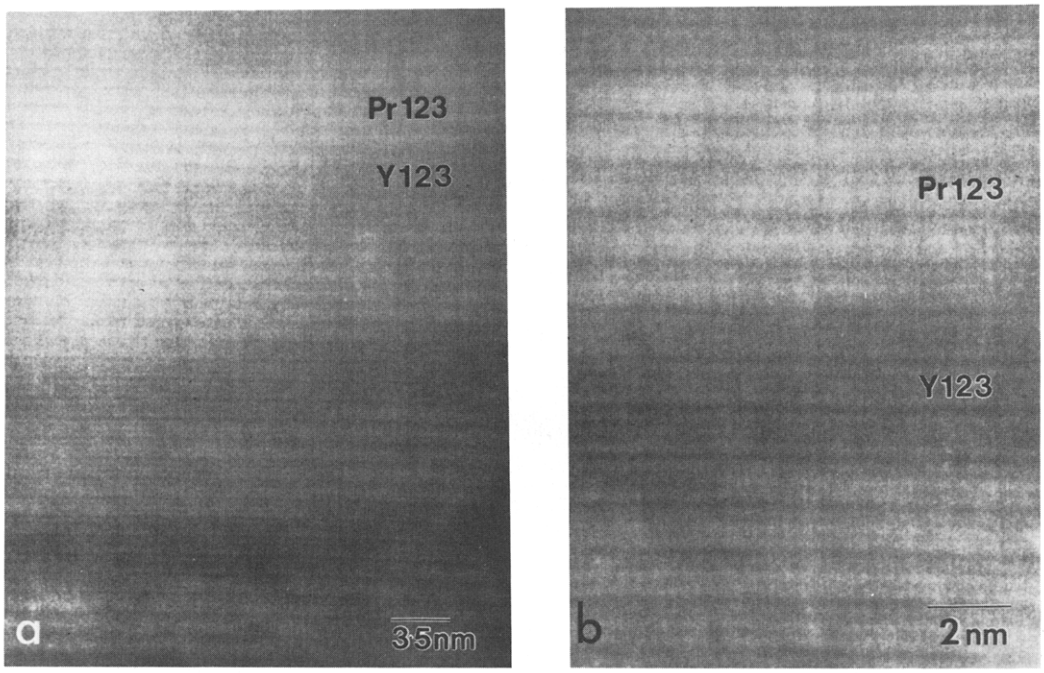

Fig. 18. Part of a $YBa_2Cu_3O_{7-x}/PrBa_2Cu_3O_{7-x}$ superlattice showing compositionally abrupt but stepped interfaces; (a) general view showing wavy compositional modulation and (b) higher magnification showing interface step.

process is similar to interrupted-growth molecular beam epitaxy, although in this case a simple growth model seems to give a good picture of the final structure which certainly does not appear to be true for the semiconductors.

Various other examples have also been discussed in a number of recent publications, including the relaxation of strained Si_xGe_{1-x} epitaxial layers, where dislocation cores were seen to reside entirely within the Ge layer [80], the imaging of defects and interfaces in $YBa_1Cu_3O_{7-x}$ thin films [81] and a study of the structure and composition of low-angle grain boundaries in $YBa_1Cu_3O_{7-x}$ [82].

6. Conclusions

The Z-contrast technique described here represents a new approach to the high-resolution imaging of crystals, providing strong compositional sensitivity in an image which to a very good approximation represents an ideal incoherent image on the atomic scale. No contrast reversals occur with specimen thickness or objective lens defocus, and no Fresnel fringe effects occur at interfaces. These effects all arise because only *s*-type Bloch states contribute significantly to the intensity at the atom sites, which is where the scattering to the high-angle detector takes place. Interference effects with other Bloch states are therefore filtered out, which allows the imaging process to be described as a simple convolution between an effective probe intensity profile and the thickness-integrated *s*-state intensity at the atom sites. The essential form of the image can be predicted and interpreted intuitively if an optimum probe is used, or may be simulated to high accuracy including the second-order thickness behavior of different atomic strings by the convolution method.

The major advantage of the technique is that each object has essentially only one possible image, which is obtained using a probe condition which does not depend on the anticipated specimen structure. The image is therefore equally sensitive to unexpected interface structures as it is to the anticipated structure. This has been illustrated by a number of practical examples showing the insights that can be obtained into materials growth processes and resulting materials properties.

The development of a 300 kV STEM with an anticipated Scherzer optimum probe size of 1.4 Å is currently in progress. Such an instrument would provide, for example, sublattice sensitivity in semiconductor materials along several major axes (see fig. 7), as well as extend our range of materials to include smaller lattices such as metals. Advances in detector sensitivity and image processing are also anticipated, together with efforts to correlate the Z-contrast image with spectroscopic analysis using localized inelastic excitations, providing a true column-by-column analytical capability. Of course, microdiffraction and phase-contrast imaging are also available if desired. It would seem, therefore, that analytical electron microscopy and high-resolution imaging could finally merge on a single instrument. This could be used on a simple intuitive level for rapidly surveying large areas or large numbers of samples giving quite considerable insight into their behavior, or at a much deeper level for extracting the maximum information from particular critical regions. There seems no doubt that the advent of high-resolution Z-contrast imaging can only increase the demand for electron microscopy in all areas of materials science.

Acknowledgments

We should like to thank M.F. Chisholm, P. Rez, D.M. Bird, J. Silcox, and C.J. Rossouw for useful discussions, I.M. Baker for provision of the Ni_3Al sample, S.M. Yalisove for provision of the $CoSi_2$ film, J.-M. Baribeau and D.C. Houghton for provision of the ultrathin SiGe superlattices, G. Robinson for provision of the quantum wells, D.H. Lowndes and D.P. Norton for the superconductor superlattices, and T.C. Estes, J.T. Luck and S.L. Carney for technical assistance. This research was sponsored by the Division of Materials Sciences, US Department of Energy, under contract DE-AC05-84OR21400 with Martin Marietta Energy Systems, Inc. and in part by an appointment to the US Department of Energy Postgraduate

Research Program at ORNL administered by Oak Ridge Associated Universities.

References

[1] A.V. Crewe and J. Wall, J. Mol. Biol. 48 (1970) 375.
[2] A.V. Crewe, J.P. Langmore and M.S. Isaacson, in: Physical Aspects of Electron Microscopy and Microbeam Analysis, Eds. B.M. Siegel and D.R. Beaman (Wiley, New York, 1975) p. 47.
[3] A. Engel, J.W. Wiggins and D.C. Woodruff, J. Appl. Phys. 45 (1974) 2739.
[4] M.S. Isaacson, M. Ohtsuki and M. Utlaut, in: Introduction to Analytical Electron Microscopy, Eds. J.J. Hren, J.I. Goldstein and D.C. Joy (Plenum Press, New York, 1979) p. 343.
[5] A.V. Crewe, Rep. Prog. Phys. 43 (1980) 621.
[6] E. Zeitler and M.G.R. Thomson, Optik 31 (1970) 258.
[7] J.M. Cowley, Ultramicroscopy 2 (1976) 3.
[8] J.M. Cowley, in: Principles of Analytical Electron Microscopy, Eds. D.C. Joy, A.D. Romig, Jr. and J.I. Goldstein (Plenum Press, New York, 1986) p. 77.
[9] J.C.H. Spence and J.M. Cowley, Optik 50 (1978) 129.
[10] A. Howie, J. Microscopy 117 (1979) 11.
[11] M.M.J. Treacy and S.B. Rice, J. Microscopy 156 (1989) 211.
[12] S.J. Pennycook, S.D. Berger and R.J. Culbertson, J. Microscopy 144 (1986) 229.
[13] S.J. Pennycook, Ultramicroscopy 30 (1989) 58.
[14] C.R. Hall and P.B. Hirsch, Proc. Roy. Soc. A 286 (1965) 158.
[15] C.R. Hall, Phil. Mag. 12 (1965) 815.
[16] Z.L. Wang and J.M. Cowley, Ultramicroscopy 31 (1989) 437; 32 (1990) 275.
[17] Z.L. Wang, Phys. Rev. B 41 (1990) 12818.
[18] P. Rez, C.J. Humphreys and M.J. Whelan, Phil. Mag. 35 (1977) 81.
[19] J. Gjonnes and R. Hoier, Acta Cryst. A 27 (1971) 166.
[20] C.J. Rossouw, Ultramicroscopy 16 (1985) 241.
[21] C.J. Rossouw and L.A. Bursill, Acta Cryst. A 41 (1985) 320.
[22] D.M. Bird and A.G. Wright, Acta Cryst. A 45 (1989) 104.
[23] H. Yoshioka, J. Phys. Soc. Jpn. 12 (1957) 618.
[24] D.M. Bird and Q.A. King, Acta Cryst. A 46 (1990) 202.
[25] C.J. Humphreys, Rep. Prog. Phys. 42 (1979) 1825.
[26] P.A. Doyle and P.S. Turner, Acta Cryst. A 24 (1968) 390.
[27] G. Radi, Acta Cryst. A 26 (1970) 41.
[28] B.F. Buxton and J.E. Loveluck, J. Phys. C 10 (1977) 3941.
[29] C.J. Humphreys and P.B. Hirsch, Phil. Mag. 18 (1968) 115.
[30] D.E. Jesson and S.J. Pennycook, in preparation.
[31] S. Takagi, J. Phys. Soc. Jpn. 13 (1958) 278.
[32] E. Zeitler and H. Olsen, Phys. Rev. B 162 (1967) 1439.
[33] H. Fleischmann, Z. Naturforsch. 15a (1960) 1090.
[34] M.M.J. Treacy, J. Microsc. Spectrosc. Electron. 7 (1982) 511.
[35] D.M. Bird, J. Electron Microsc. Tech. 13 (1989) 77.
[36] J.C.H. Spence, J.M. Zuo and J. Lynch, Ultramicroscopy 32 (1989) 233.
[37] D.E. Jesson, S.J. Pennycook and M.F. Chisholm, in: Atomic Scale Structure of Interfaces, Eds. R.D. Bringans, R.M. Feenstra and J.M. Gibson (Materials Research Society, Pittsburgh, 1990) p. 439.
[38] D.E. Jesson and S.J. Pennycook, in: Proc. 12th Int. Congr. for Electron Microscopy, Vol. 1, Eds. L.D. Peachey and D.B. Williams (San Francisco Press, San Francisco, 1990) p. 74; and Ultramicroscopy, submitted.
[39] D.H. Shin, E.J. Kirkland and J. Silcox, Appl. Phys. Lett. 55 (1989) 2456.
[40] P. Xu, E.J. Kirkland, J. Silcox and R. Keyse, Ultramicroscopy 32 (1990) 93.
[41] E.J. Kirkland, R.F. Loane and J. Silcox, Ultramicroscopy 23 (1987) 77.
[42] R.F. Loane, E.J. Kirkland and J. Silcox, Acta Cryst. A 44 (1988) 912.
[43] R.F. Loane and J. Silcox, in: Proc. 12th Int. Congr. for Electron Microscopy, Vol. 4, Eds. L.D. Peachey and D.B. Williams (San Francisco Press, San Francisco, 1990) p. 396.
[44] A. Howie, Phil. Mag. 14 (1967) 223.
[45] K. Kambe, G. Lehmpfuhl and F. Fujimoto, Z. Naturforsch. 29a (1974) 1034.
[46] A. Ichimiya and G. Lehmpfuhl, Z. Naturforsch. 33a (1978) 269.
[47] P.B. Hirsch, A. Howie and M.J. Whelan, Phil. Mag. 7 (1962) 2095.
[48] D. Cherns, A. Howie and M.H. Jacobs, Z. Naturforsch. 28a (1973) 565.
[49] J. Tafto, Z. Naturforsch. 34a (1979) 452.
[50] C.J. Rossouw and V.W. Maslen, Ultramicroscopy 21 (1987) 277.
[51] S.J. Pennycook and A. Howie, Phil. Mag. 41 (1980) 809.
[52] S.J. Pennycook and D.E. Jesson, Phys. Rev. Lett. 64 (1990) 938.
[53] B.F. Buxton, J.E. Loveluck and J.W. Steeds, Phil. Mag A 38 (1978) 259.
[54] R. Vincent, D.M. Bird and J.W. Steeds, Phil. Mag. A 50 (1984) 765.
[55] K. Kambe, Ultramicroscopy 10 (1982) 223.
[56] J. Fertig and H. Rose, Optik 59 (1981) 407.
[57] D.E. Jesson, S.J. Pennycook and J.-M. Baribeau, in: High Resolution Electron Microscopy of Defects in Materials, Eds. R. Sinclair, D.J. Smith and U. Dahmen (Materials Research Society, Pittsburgh, 1990) p. 223.
[58] A.M. Ozorio de Almeida, Acta Cryst. A 31 (1975) 435.
[59] B.F. Buxton and P.T. Tremewan, Acta Cryst. A 36 (1980) 304.
[60] M. Born and E. Wolf, in: Principles of Optics, 6th Ed. (Pergamon Press, Oxford, 1980) pp. 333 and 415.
[61] O. Scherzer, J. Appl. Phys. 20 (1949) 20.

[62] A.V. Crewe and D.B. Salzman, Ultramicroscopy 9 (1982) 373.
[63] J.M. Cowley, in: High Resolution Transmission Electron Microscopy, Eds. P.R. Buseck, J.M. Cowley, and L. Eyring (Oxford University Press, New York, 1988) p. 3.
[64] C. Mory, C. Colliex and J.M. Cowley, Ultramicroscopy 21 (1987) 171.
[65] I.M. Baker, E.M. Schulson, J.R. Michael and S.J. Pennycook, Phil. Mag. B 62 (1990) 659.
[66] M.J. Hafich, J.H. Quigley, R.E. Owens, G.Y. Robinson, Du Li and N. Otsuka, Appl. Phys. Lett. 54 (1989) 2586.
[67] S.J. Pennycook, D.E. Jesson and M.F. Chisholm, in: Nanostructures and Microstructure Correlation with Physical Properties of Semiconductors, Eds. H.G. Craighead and J.M. Gibson (SPIE, Bellingham, 1990) p. 182.
[68] S.M. Yalisove, R.T. Tung and D. Loretto, J. Vac. Sci. Technol. A 7 (1989) 1472.
[69] D. Loretto, J.M. Gibson and S.M. Yalisove, Phys. Rev. Lett. 63 (1989) 298.
[70] R.J. Hamers, U.K. Kohler and J.E. Demuth, J. Vac. Sci. Technol. A 8 (1990) 195.
[71] H. Niehus, U.K. Kohler, M. Copel and J.E. Demuth, J. Microscopy 152 (1988) 753.
[72] J.-M. Baribeau, T.E. Jackman, P. Maigne, D.C. Houghton and M.W. Denhoff, J. Vac. Sci. Technol. A 5 (1987) 1898.
[73] P.B. Littlewood, Phys. Rev. B 34 (1986) 1363.
[74] A. Ourmazd and J.C. Bean, Phys. Rev. Lett. 55 (1985) 765.
[75] F.K. LeGoues, V.P. Kesan and S.S. Iyer, Phys. Rev. Lett. 64 (1990) 40.
[76] F.K. LeGoues et al., Phys. Rev. Lett. 64 (1990) 2038.
[77] D.E. Jesson, S.J. Pennycook and J.-M. Baribeau, Phys. Rev. Lett. 66 (1991) 750.
[78] D.J. Chadi, Phys. Rev. Lett. 59 (1981) 1691.
[79] D.H. Lowndes, D.P. Norton and J.D. Budai, Phys. Rev. Lett. 65 (1990) 1160.
[80] M.F. Chisholm, S.J. Pennycook and D.E. Jesson, in: Atomic Scale Structure of Interfaces, Eds. R.D. Bringans, R.M. Feenstra and J.M. Gibson (Materials Research Society, Pittsburgh, 1990) p. 447.
[81] S.J. Pennycook, M.F. Chisholm, D.E. Jesson, D.P. Norton, J.W. McCamy and D.H. Lowndes, in: High-Temperature Superconductors: Fundamental Properties and Novel Materials Processing, Eds. D.K. Christen, J. Narayan and L. Schneemeyer (Materials Research Society, Pittsburgh, 1990) p. 765.
[82] M.F. Chisholm and S.J. Pennycook, in: Proc. 47th Annu. EMSA Meeting, Ed. G.W. Bailey (San Francisco Press, San Francisco, 1989) p. 198.